POLITECNICO DI TORINO
Repository ISTITUZIONALE

Engineering Deformation and Failure in Diamond Triply Periodic Minimal Surface Lattices via 3D Wall Thickness Grading

Original
Engineering Deformation and Failure in Diamond Triply Periodic Minimal Surface Lattices via 3D WallThickness Grading / Rizza, G., Bruson, D., Galati, M., Iuliano, L.. - In: ADVANCED ENGINEERING MATERIALS. - ISSN 1527-2648. - ELETTRONICO. - 28:5(2026). [10.1002/adem.202502812]

Availability:
This version is available at: 11583/3009839 since: 2026-04-13T14:49:19Z

Publisher:
John Wiley and Sons Inc

Published
DOI:10.1002/adem.202502812

Terms of use:

This article is made available under terms and conditions as specified in the corresponding bibliographic description in the repository

Publisher copyright

(Article begins on next page)

07 November 2026

Check for updates

ADVANCED ENGINEERING MATERIALS
www.aem-journal.com

Engineering Deformation and Failure in Diamond Triply Periodic Minimal Surface Lattices via 3D Wall-Thickness Grading

Giovanni Rizza, Danilo Bruson, Manuela Galati, and Luca Iuliano*

Among the different lattice structures, the one based on triply periodic minimal surface (TPMS) is characterized by the absence of sharp angles, which guarantees superior mechanical properties if compared to beam-based structures. The mechanical response of these structures depends on the geometry of the guiding surface and the wall thickness, which is typically considered constant throughout the structure. On the contrary, this work investigates the modulation of the mechanical response of the diamond TPMS structure through the graduation of the wall thickness, with four different patterns: vertical, diagonal, cross, and core. For each of these structures, samples are produced with the powder bed fusion with electron beam additive manufacturing technique. Morphological characteristics of the structures are measured using X-ray computed tomography. These data are then correlated to the mechanical properties obtained from compression tests and the deformation behavior obtained from digital image correlation analyses. The results show that 3D wall thickness gradation can be successfully adopted to modulate the mechanical and deformation behavior of the structures. Moreover, structures with a graded wall thickness provide improved energy absorption capabilities and show the possibility to tune energy absorption as a function of the adopted gradation pattern and thickness.

1. Introduction

Lattice structures replicate what is visible in numerous examples in nature: microstructures of metals, bones of animals, stems of plants, or honeycomb structures created by bees. Lattice structures are characterized by lightness, mechanical strength,[1] excellent energy absorption capabilities,[2] tunable thermal behavior,[3] and noise suppression capabilities.[4]

A lattice structure is formed by an arrangement in the 3D space of a unit cell. This arrangement can be random, periodic, or pseudoperiodic.[5] In random structures, the unit cells are randomly distributed in space. Periodic structures have unit cells arranged in a repeating pattern in space. The pseudoperiodic structures exhibit a periodic distribution of cells of varying sizes in space. Besides the classification based on the distribution of cells, another classification is usually adopted in the literature based on the design of the unit cell. Lattice structures are typically classified into two families: strut-based and surface-based.[6] Strut-based lattices are composed of several struts connected at nodes. The surface-based unit cell is defined as a series of points equidistant from a guiding surface, which is obtained by offsetting the reference surface.[7] The maximum distance between these points is typically called the wall thickness. Among the guiding surfaces, the triply periodic minimal surfaces (TPMS) are not self-intersecting surfaces, characterized by a zero-mean curvature at each point and repeat periodically in three independent spatial directions.[8] The absence of sharp angles or nodes, combined with a smooth and continuous surface, ensures a reduction of stress concentration and increased mechanical resistance.[9] Structures based on TPMS find applications in several engineering fields, as discussed in the review proposed by Li et al.[10] In functional components, they showed good energy absorption properties[11,12] and the capability to reduce weight, stresses, and deformations in components, such as turbine blades.[13] In heat exchangers, these geometries produce a turbulent flow, which improves the exchange capabilities.[14] Mimicking what is observed in nature, structures based on TPMS surfaces find several applications in scaffolds for biomedical implants, where the tuneability of the structure porosities improves properties such as bone proliferation and osteointegration.[15] Leveraging the large specific surface area, structures based on TPMS find applications also as catalyst structures for the generation of hydrogen[16] or as key geometries for microreactors for CO_2 methanation.[17]

Owing to the geometrical complexity of such structures, their manufacturability is currently limited to certain additive manufacturing (AM) processes, particularly those involving metallic materials. Among the available AM technologies,

G. Rizza, D. Bruson, M. Galati, L. Iuliano
Department of Management and Production Engineering (DIGEP)
Integrated Additive Manufacturing Center (IAM@PoliTo)
Politecnico di Torino
Corso Duca degli Abruzzi 24, 10129 Torino, Italy
E-mail: danilo.bruson@polito.it

The ORCID identification number(s) for the author(s) of this article can be found under https://doi.org/10.1002/adem.202502812.

© 2026 The Author(s). Advanced Engineering Materials published by Wiley-VCH GmbH. This is an open access article under the terms of the Creative Commons Attribution License, which permits use, distribution and reproduction in any medium, provided the original work is properly cited.

DOI: 10.1002/adem.202502812

15272648, 2026, 5, Downloaded from https://advanced.onlinelibrary.wiley.com/doi/10.1002/adem.202502812 by Politecnico Di Torino Sist. Bibl Del Polit Di Torino, Wiley Online Library on [13/04/2026]. See the Terms and Conditions (https://onlinelibrary.wiley.com/terms-and-conditions) on Wiley Online Library for rules of use; OA articles are governed by the applicable Creative Commons License

powder bed fusion with electron beam (PBF-EB) stands out for its capability to handle complex structures, thanks to the hot build environment. The high temperature in the build chamber produces partial sintering among the unmelted powder particles.[18] The sintering among the particles increases the thermal conductivity of the unmelted material,[19] promoting the dissipation of the heat generated during melting and improving the thermal stability of the powder bed. This allows the production of complex structures with a reduced number of support structures, or, as in the case of strut-based and surface-based lattice structures, without supports.[20] However, the peculiar characteristics of the PBF-EB process involving sintering and the electron beam diameter (which is larger than a laser beam) pose limitations to the minimum wall thickness dimension and the channels created by the surfaces. It has been shown in the literature that, depending on the beam parameters, the minimum beam diameter for the PBF-EB is ≈400 μm.[18] Besides the minimum beam diameter, other processing factors, such as the interaction between the electron beam and the powder, the beam speed, the beam current, or the focus offset, may affect the quantity of melted material. The interaction of these parameters results in structures that, despite being designed with a reduced thickness (e.g., 100 μm,[21,22] typically have a wall thickness that is larger than 350 μm.[21,22] Another limitation when producing such structures using the PBF-EB is the removal of the sintered powder. The standard cleaning procedure for PBF-EB parts involves removing the sintered powder by blasting the parts in the powder recovery system (PRS) using the same powder used for production. However, this procedure implies that the media can access the voids of all the structures through its channels. Therefore, the possibility of removing the powder depends on the diameter of the channels, the wall thickness, and the width of the structure.[22] Despite these process limitations, the literature on TPMS structures produced by PBF-EB is increasing.[21–28] However, the geometries investigated are limited. To the best of the authors' knowledge, only Sokollu et al.[19] and Bol and Ramulu[20] have considered the diamond surface-based structure, with a constant wall thickness.

From the point of view of the mechanical response, the lattice structures are typically analyzed under compression,[29] following the prescription of the ISO 13314:2011[30] for stochastic cellular materials. Commonly, the relative density of the structure is used as a descriptor of mechanical properties. However, it has been demonstrated that other factors, including cell geometry, material, and wall thickness, also influence the mechanical properties of lattice structures. Tailoring the wall thickness within the structure could open new possibilities to modulate the mechanical response and tune the deformation behavior of the structure.[31] A first result that shows the feasibility of such an approach was presented by Bol and Ramulu,[28] in which a four-point bending test of a sandwich diamond TPMS structure with a topology optimized wall thickness showed that wall-thickness grading according to the stress distribution can produce structures up to 50% stronger than uniform wall thickness structures.

This work focuses on diamond TPMS surface-based lattice structures and investigates the effect of different 3D grading patterns on mechanical response and deformation behavior under compression. The patterns are three-dimensional, and therefore the grading is designed along three main directions.

2. Methodology

2.1. Design of the Structures

The focus of this work is the lattice structure based on the Swartz diamond TPMS surface. In general, TPMS are characterized by an average null curvature at each point. These surfaces are also periodic and infinite. One possible way to define the nodal coordinates of a minimal surface is to use the level set approximation equations. These equations are trigonometric functions that satisfy the condition $\varphi(x, y, z) = t(x, y, z)$, where the function $\varphi(x, y, z)$ describes a surface calculated at the iso value $t(x, y, z)$.[32,33] Equation (1) represents the level set approximation equation adopted to describe the Swartz diamond lattice structure adopted in this work.

$$\begin{aligned}\varphi(x,y,z) = {} & \sin\left(\frac{2\pi}{L_x}x\right)\sin\left(\frac{2\pi}{L_y}y\right)\sin\left(\frac{2\pi}{L_z}z\right) \\ & + \sin\left(\frac{2\pi}{L_x}x\right)\cos\left(\frac{2\pi}{L_y}y\right)\cos\left(\frac{2\pi}{L_z}z\right) \\ & + \cos\left(\frac{2\pi}{L_x}x\right)\sin\left(\frac{2\pi}{L_y}y\right)\cos\left(\frac{2\pi}{L_z}z\right) \\ & + \cos\left(\frac{2\pi}{L_x}x\right)\cos\left(\frac{2\pi}{L_y}y\right)\sin\left(\frac{2\pi}{L_z}z\right) \\ & = t(x,y,z)\end{aligned} \tag{1}$$

where L_x, L_y, and L_z are the dimensions of the unit cell in the x, y, and z directions of the space, respectively. When the level set equation $\varphi(x, y, z)$ is evaluated at $t(x, y, z) = 0$, the result is a surface in the 3D space. The lattice cell based on this surface is obtained in this work by considering the solid volume included in the offset of the TPMS surface, so that $-t(x, y, z) < \varphi(x, y, z) < t(x, y, z)$. The iso value $t(x, y, z)$ is considered a function of the space coordinates. Changes in the value of this parameter are adopted to change the wall thickness of the structures. **Figure 1**a shows a representation of the unitary cell adopted.

The samples, including the different wall thickness gradation patterns, were designed using the software nTop (nTopology, New York, United States). The unit cell and the total volume of the sample were selected to allow the complete removal of the sintered powder and were equal to $10 \times 10 \times 10$ mm (Figure 1a) and $20 \times 20 \times 30$ mm, respectively. The ordered repetition in the selected volume of the unit cell resulted in a sample that included two unit cells in the X direction, two unit cells in the Y direction, and three unit cells in the Z direction. Figure 1b shows the representation of a sample adopted in this work, showing the arrangement of the twelve unit cells. The production was done with the Z-axis of the structure aligned along the build direction.

The grading pattern was obtained by varying the structure thickness from a "minimum thickness" $t_{min} = 0.7$ mm and a "maximum thickness" $t_{max} = 1.4$ mm. The graded wall thickness structures were generated by initially identifying an initiator surface. This surface, depending on the structures, may be a 2D or 3D surface crossing the volume of the sample. This surface represents the location from which the thickness grading begins.

 © 2026 The Author(s). Advanced Engineering Materials published by Wiley-VCH GmbH

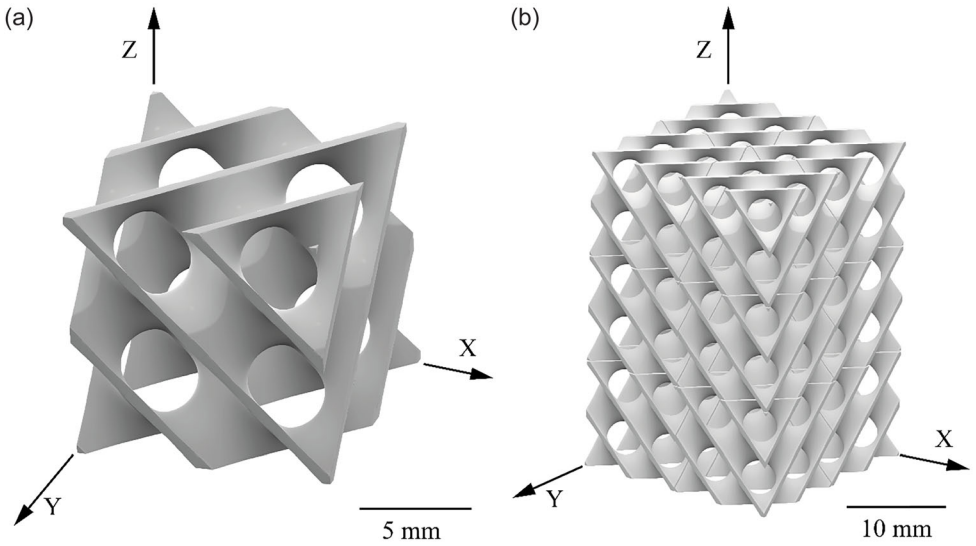


Figure 1. *Z* aligns with the build direction. a) Unit diamond cell. b) Complete sample obtained as the repetition of the unit cell in space.

Depending on the structure, the initiator surface has a thickness set to t_{min} or t_{max}. From the initiator surface, the wall thickness is linearly graded until reaching the opposite extreme value. The grading was done normally or radially to the initiator surface. For each grading pattern, two structures were designed: one with the initiator surface set at t_{min} and one with the initiator surface set at t_{max}. The structures were identified with the letter D to indicate that the TPMS surface considered is a diamond. This is followed by one or two letters to identify the grading pattern and a number to identify the thickness at the initiator surface. 1 was adopted for t_{min}, while 2 was adopted for t_{max}. Two structures with a constant wall thickness equal to t_{min} and t_{max} were designed and served as reference structures when considering the effect of the graded wall thickness. The relative density of the structure is defined as the ratio of the volume of solid material to the volume of the sample. The considered grading patterns were, therefore: 1) Uniform thickness (UT). Structures with a uniform wall thickness. DUT1 is the structure with a wall thickness of 0.7 mm and a relative density of 23.5%. DUT2 is the structure with a wall thickness of 1.4 mm and a relative density of 46.9%. 2) Vertical (V). Indicates structures with the initiator surface positioned perpendicular to the *z*-axis of the structure at the center of the structure. The thickness was linearly varied in both directions, $+z$ and $-z$, parallel to the build direction. DV1 is characterized by an initiator surface with a thickness of 0.7 mm and a nominal relative density of 34.8%. DV2 has an initiator surface with a thickness of 1.4 mm and a relative density of 35.5%. 3) Diagonal (D). For these structures, the initiator surface is tilted 45° with respect to the build direction, oriented along the diagonal of the sample considered. The wall thickness is graded orthogonally to this surface toward the edges of the sample. DD1 is characterized by an initiator surface with a thickness of 0.7 mm and a relative density of 36.3%. DD2 has an initiator surface with a wall thickness of 1.4 mm and is characterized by a relative density of 34.0%. 4) Cross (X). The initiator surface of this structure is composed of two diagonal planes tilted 45° counterclockwise and clockwise from the build direction. The thickness is normally varied from the initiator surfaces. The DX1 has two initiator surfaces of 0.7 mm and is characterized by a relative density of 30.8%. The DX2 sample has two initiator surfaces with a thickness of 1.4 mm and is characterized by a relative density of 39.4%. 5) Core (C). The initiator surface for these structures is composed of a sphere with a diameter of 17 mm positioned at the barycenter of the structure. The wall thickness is graded linearly toward the center of the sphere. Outside the sphere, the wall thickness of the structure is considered constant and equal to the thickness at the initiator surface. In DC1, the initiator surface has a thickness of 0.7 mm and a relative density of 44.7%. The structure identified as DC2 has an initiator surface with a thickness of 1.4 mm and a relative density of 25.6%.

Figure 2 shows the position of the initiator surface for the different structures considered.

2.2. Manufacturing

For the production, the samples were exported from the CAD nTop as STL files and imported into the CAM Magics (Materialize, Leuven, Belgium), which was used for the build preparation. As discussed in Section 2.1, the samples were positioned with the *Z*-axis aligned to the build direction and rotated by 45° around the *Z*-axis. Three replicas for each sample were included in the build for a total of 30 samples. The samples were positioned directly attached to the start plate, which has a size of 210×210 mm. The location of the samples on the start plate was randomized to avoid any systematic effect on their properties, ensuring a distance of at least 8 mm between adjacent samples to prevent any heat interaction. The production was conducted using the Arcam A2X machine (Colibrium additive, a GE aerospace company, Mölnlycke, Sweden) and a standard Ti6Al4V powder, which was processed with Arcam standard process parameters.[34]

The samples produced were cleaned from the sintered powder using the PRS, a blasting process conducted with the same powder used for production.

 © 2026 The Author(s). Advanced Engineering Materials published by Wiley-VCH GmbH

15272648, 2026, 5, Downloaded from https://advanced.onlinelibrary.wiley.com/doi/10.1002/adem.202502812 by Politecnico Di Torino Sist. Bibl Del Polit Di Torino, Wiley Online Library on [13/04/2026]. See the Terms and Conditions (https://onlinelibrary.wiley.com/terms-and-conditions) on Wiley Online Library for rules of use; OA articles are governed by the applicable Creative Commons License

15272648, 2026, 5, Downloaded from https://advanced.onlinelibrary.wiley.com/doi/10.1002/adem.202502812 by Politecnico Di Torino Sist. Bibl Del Polit Di Torino, Wiley Online Library on [13/04/2026]. See the Terms and Conditions (https://onlinelibrary.wiley.com/terms-and-conditions) on Wiley Online Library for rules of use; OA articles are governed by the applicable Creative Commons License

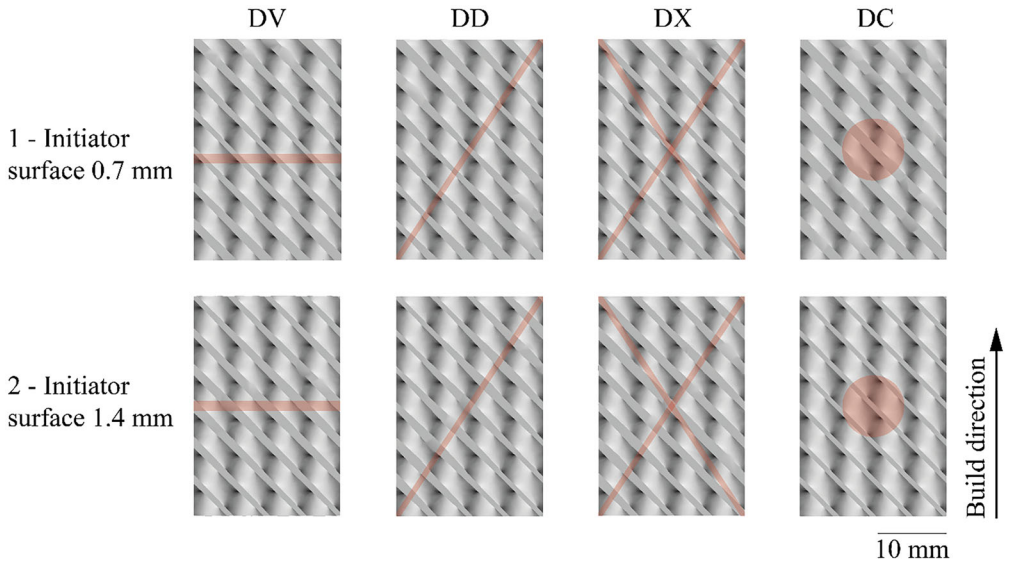


Figure 2. Grading pattern in the space of the structures. The red area represents the position of the initiator surface that is orthogonal to the figure plane. The thickness of the initiator surface is out of scale.

2.3. Characterization of Morphology

For each geometry, one sample was examined using computed tomography (CT-scan) using the GE phoenix V|tome|x S240 (GE inspection technologies, Wunstorf, Germany). To achieve the best resolution, a voltage of 140 kV and a current of 170 μA were used, with a corresponding voxel size of ≈35 μm, which allowed the capture of the entire sample in one tomography. The CT-scan data were analyzed using VGStudio Max 3.4 (Volume Graphics GmbH, Heidelberg, Germany), and the following parameters were extracted or calculated: 1) The actual volume of the samples produced after surface determination. Surface determination is a preliminary thresholding operation to distinguish between the solid material and the surrounding space. 2) The amount of enclosed porosity within the sample volume. The porosity is given as a volume expressed in mm^3. 3) The wall thickness distribution, which was determined using the sphere method. This analysis allowed the evaluation of the actual wall thickness of the samples produced. The outcome is a histogram of the thickness occurrence. The same analysis and the same histograms were also evaluated for the nominal geometries, to allow the nominal/actual wall thickness comparison. 4) The dimensional nominal/actual comparison to compare the dimensions of the actual samples to the nominal CAD file adopted for production. The alignment between the reconstruction from tomography and the CAD file was done using the best-fit algorithm. The outcome is a frequency distribution of the relative dimensional deviations, also calculated in cumulative form.

2.4. Characterization of Mechanical Properties

The mechanical and deformation behavior of the structures was characterized under a quasistatic compression load. The Easydur Aura 10T (Easydur Srl, Arcisate, Italy) universal testing machine, equipped with a 100 kN load cell, was adopted. Since no specific standards are currently available for characterizing the lattice structures produced with AM techniques, the compression tests were performed following, where possible, the indications of the ISO 13314:2011,[30] generally valid for porous materials. The displacement of the mobile crosshead was set to 2 mm min^{-1}. The stress values in the samples were evaluated as the ratio of load measured by the load cell divided by the envelop cross-section area of the structure (in this case, 20 × 20 mm). This information was adopted to plot the stress–strain curve and evaluate all the information that characterizes the structure, as suggested by ISO 13314:2011.[30] The failure of the structure was set at a strain equal to 50% of the height of the specimen. The indications provided by ISO 13314:2011[30] were also adopted for the evaluation of the quasielastic gradient (E), the first maximum compressive strength (FMCS), the plateau stress (σ_{pl}), the compressive offset stress (σ_c), and the energy absorption at 50% strain (W_{50}). It should be noted that, in accordance with ISO 13314:2011,[30] these values represent effective mechanical parameters for porous structures (e.g., quasielastic gradient), which are not identical to the conventional definitions used for bulk materials such as Young's modulus, but rather provide a meaningful counterpart that accounts for the porous architecture. The energy absorption (W_v) and energy absorption efficiency ($\eta(\varepsilon)$) were adopted to evaluate the ductility characteristics of the structures. W_v was assessed as the area subtended by the stress–strain curve between zero and the ε_{end} according to Equation (2).[35] $\eta(\varepsilon)$ is defined as the ratio between the absorbed energy at any strain value (ε) and the relative stress $\sigma(\varepsilon)$. Equation (3) represents the equation adopted to evaluate $\eta(\varepsilon)$.[36]

$$W_v = \int_0^{\varepsilon} \sigma(\varepsilon) \mathrm{d}\varepsilon \tag{2}$$

$$\eta(\varepsilon) = \frac{1}{\sigma(\varepsilon)} \int_0^{\varepsilon} \sigma(\varepsilon) \mathrm{d}\varepsilon \tag{3}$$

To enable a fair comparison among the performances of the different diamond gradations, utilizing specific values per unit

 © 2026 The Author(s). Advanced Engineering Materials published by Wiley-VCH GmbH

15272648, 2026, 5, Downloaded from https://advanced.onlinelibrary.wiley.com/doi/10.1002/adem.202502812 by Politecnico Di Torino Sist. Bibl Del Polit Di Torino, Wiley Online Library on [13/04/2026]. See the Terms and Conditions (https://onlinelibrary.wiley.com/terms-and-conditions) on Wiley Online Library for rules of use; OA articles are governed by the applicable Creative Commons License

mass, the quasielastic gradient (related to rigidity) and the (FMCS related to strength) were normalized by the product of the actual relative density and bulk density of the base material (4420 kg m^{-3}[37]), yielding specific values per unit mass (E_{spec} and $FMCS_{spec}$). The specific energy absorption (SEA) is then used as an index for the crashworthiness of the structures and is calculated as the ratio between W_{50} and the specimen mass. The performed normalization ensures that the mechanical responses can be directly compared across specimens with different global densities, so that the observed differences are attributable to the grading pattern and internal geometry rather than to density variations.

Each produced sample was tested under compression, and the data collected for each geometry from the three replicas tested were averaged to extract the stress–strain curve and the mechanical properties of the structure. While the compression tests evaluate the performance, a detailed investigation of the strain evolution was conducted through Digital Image Correlation (DIC). The use of DIC enabled full-field strain measurements across the specimen surface, allowing for a quantitative assessment of localized deformation, strain distribution heterogeneity, and the onset and propagation of failure. Particular attention was paid to the identification of the region of interest (ROI) and the strain field analysis at the (ε_{FMCS}). The complete DIC methodology, including image acquisition, speckle pattern evaluation, and subset selection, is described in detail in Appendix A.

2.5. Surface Topography and Fracture Analysis

The surface topography of the DD1 sample was inspected using the JCM6000 plus scanning electron microscope (SEM) from JEOL (JEOL Ltd., Tokyo, Japan). Moreover, after the compression test, the fracture surface was inspected using the S9i microscope from Leica (Leica Microsystems GmbH, Wetzlar, Germany) and the JCM6000 SEM. The surface topography was inspected to identify surface characteristics that could promote the sample fracture or affect the dimensional wall thickness accuracy. The analysis of the fracture surface, instead, allows for the evaluation of the fracture mode in the specific case of the DD1 sample, a sample that failed in a brittle manner.

3. Results

3.1. Characterization of Morphology

Figure 3 illustrates the outcomes calculated from tomographic analyses related to actual relative density, volumetric deviation, and the presence of internal closed porosity, i.e., referred to as pores or voids trapped inside the solid material regions of the TPMS bulk walls that result from incomplete melting, gas entrapment, or lack of fusion during the AM process. In Figure 3, moving from left to right along the *x*-axis, the structures are ordered by increasing the actual relative density (blue dotted line in Figure 3). Overall, the specimens exhibited a minimal occurrence of enclosed small pores (green line in Figure 3), with a material density exceeding 99.99%, as evidenced in Figure 3, where the porosity across all samples remained below 0.002%. At this threshold, the material can be considered as effectively fully dense, with negligible internal voids affecting structural integrity.[38] Slight differences were found in the porosity of the samples. DV1, DV2, DD1, DX2, DC1, and DUT2 present a porosity comprised between ≈0.001% and 0.0013% whereas DUT1, DC2, DX1, and DD2 exhibited slightly higher porosity values, exceeding 0.0015%.

The data about volume percentage deviation, reported in the red line in Figure 3, shows that the fabricated samples were consistently smaller than their nominal counterparts. This discrepancy may be attributed to the absence of any geometric compensation in the design phase to account for shrinkage during cooling. Accurately predicting and correcting for such shrinkage, especially in thin-walled structures with varying thicknesses, remains a significant challenge. As shown in Figure 3, the

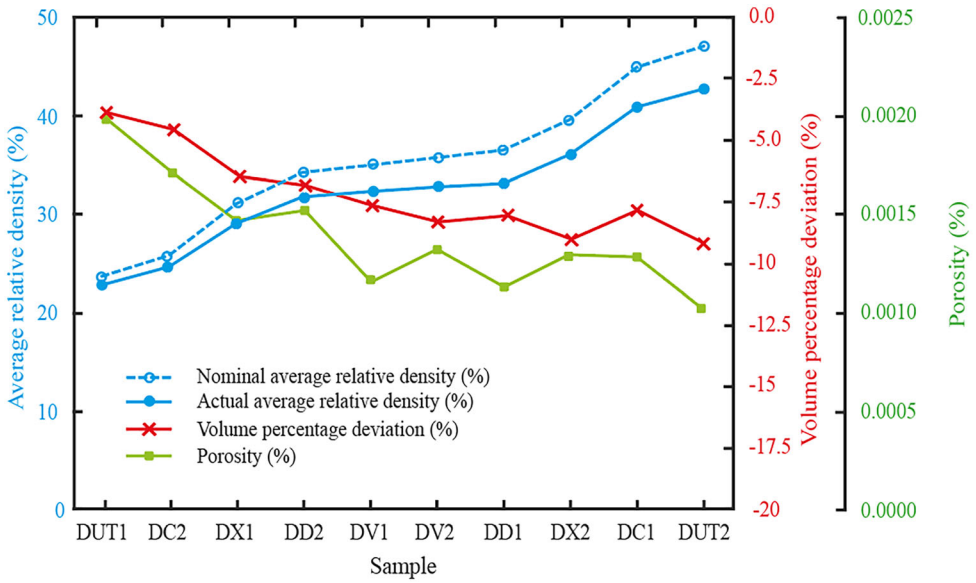


Figure 3. Results of the average nominal/actual relative densities, actual volume percentage differences from nominal STL, and porosity of the samples.

 © 2026 The Author(s). Advanced Engineering Materials published by Wiley-VCH GmbH

percentage deviation in volume relative to the nominal design increases with both the average relative density and the associated wall thickness. The data about the actual relative density (blue line in Figure 3) shows a similar trend. The produced samples had a density systematically lower than the nominal. The percentage difference ranges from −3.8% for DUT1 to −9.3% for DUT2. These represent the smallest and largest values, with all other samples having a deviation within this range.

Figure 4 shows an example of the deviation and wall thickness analysis conducted on samples DX2 and DUT2, respectively. The analysis of the volume of the fabricated samples and the relative density can be further extended by considering the actual wall thicknesses of the structures.

The highest deviations comparing the actual geometry to the nominal geometry, ≈0.9 mm, are located at the base of the sample, where the sample is attached to the start plate (marked in red in the colormap of Figure 4a), followed by a rapid decrease toward small deviations (green areas in Figure 4a). The direct connection of the samples on the start plate may have influenced the thermal behavior during the initial stages of fabrication and subsequent cooling, leading to localized shrinkage effects.[39,40] The thermal influence of the start plate, which behaves as a thermal basin, can induce thermally driven distortions, such as positive deviations in geometry or slight warping of the deposited layers perpendicular to the build direction, resulting in negative deviations[41] leading to consistently lower heights of the samples than the nominal 30 mm. This reduction indicates geometric deformation along the build axis due to thermal inhomogeneities during the process, particularly due to non-uniform temperature distribution near the start plate along the build direction.[42]

Figure 5 compares the wall thickness distributions derived from the reference STL files (nominal CAD design) with those obtained from CT-scan reconstructions (actual produced structure). The peaks in these distributions represent the most frequently occurring thicknesses within each structure. **Table 1** reports the mean (*M*) and relative standard deviation (SD) for the produced samples compared to the data obtained from nominal CAD files. As shown in Figure 5, all structures exhibit a slight leftward shift in the wall thickness distribution compared to the nominal distribution, indicating that the characteristic wall thickness of the structure is consistently smaller than the designed value. While the STL-based distributions display well-defined dominant thicknesses (represented by sharp peaks in the black curves of Figure 5), the fabricated structures show a more gradual variation, with increased variance and a smaller mean (Table 1). The actual distributions are broader than those of the STL models, with minimum wall thicknesses smaller and maximum wall thicknesses larger than the nominal values. This wider distribution suggests the presence of regions with thicknesses exceeding the nominal values. Such deviations are consistent with the typical characteristics of the PBF-EB process, where surface roughness and partially sintered powder particles, particularly on down-skin surfaces, contribute to irregularities in wall thickness.[34]

In the case of the structure with uniform wall thickness with nominal values of 0.7 mm for DUT1 and 1.4 mm for DUT2, the actual measurements revealed less pronounced peaks and broader distributions. Moreover, the peak occurs at a smaller wall thickness than the designed one. Also, graded structures exhibited less pronounced peaks, corresponding to intermediate thicknesses between the designed minimum and maximum values. In fact, the average values of the wall thickness distributions display increasing absolute percentage differences between the nominal and actual geometries as the relative density increases. Specifically, as reported in Table 1, DUT1 shows the smallest deviation, ≈−1.5%, which progressively increases up to −8% for specimens with a relative density above 35%. This trend is consistent with the volumetric deviation pattern previously discussed. Furthermore, all distributions display right-skewed tails in the CT-scan data (actual geometries), indicating the presence of thicker regions compared to the nominal STL models. These thicker regions are attributed to the material accumulation observed at the junctions where the surfaces adjacent to the

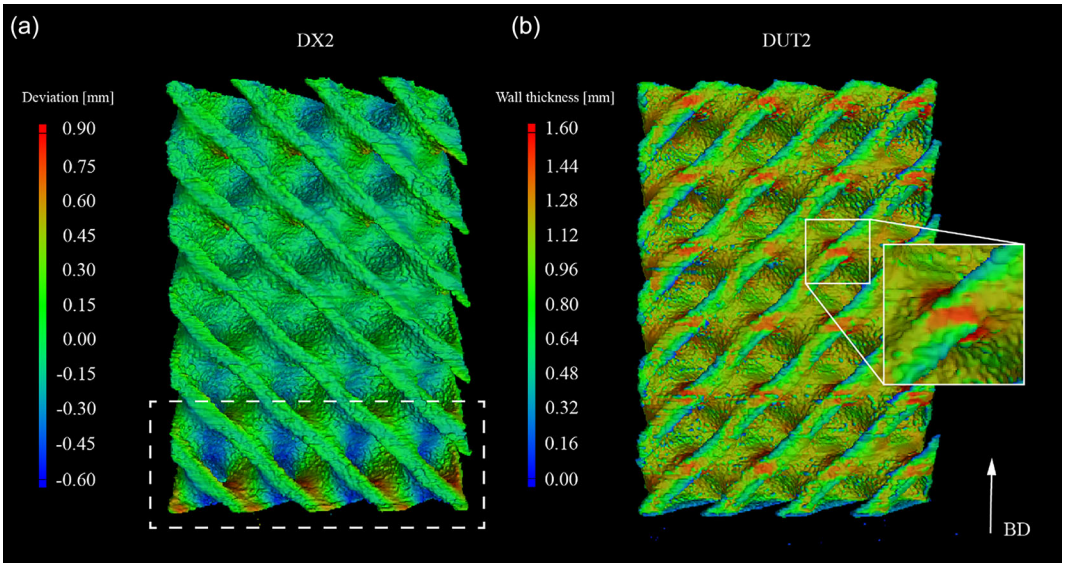


Figure 4. Example of a) nominal/actual comparison and b) wall thickness analysis for the structures DX2 and DUT2, with high deviation and high wall thickness regions highlighted in the analysis contour plots. BD refers to the building direction.

© 2026 The Author(s). Advanced Engineering Materials published by Wiley-VCH GmbH

15272648, 2026, 5, Downloaded from https://advanced.onlinelibrary.wiley.com/doi/10.1002/adem.202502812 by Politecnico Di Torino Sist. Bibl Del Polit Di Torino, Wiley Online Library on [13/04/2026]. See the Terms and Conditions (https://onlinelibrary.wiley.com/terms-and-conditions) on Wiley Online Library for rules of use; OA articles are governed by the applicable Creative Commons License

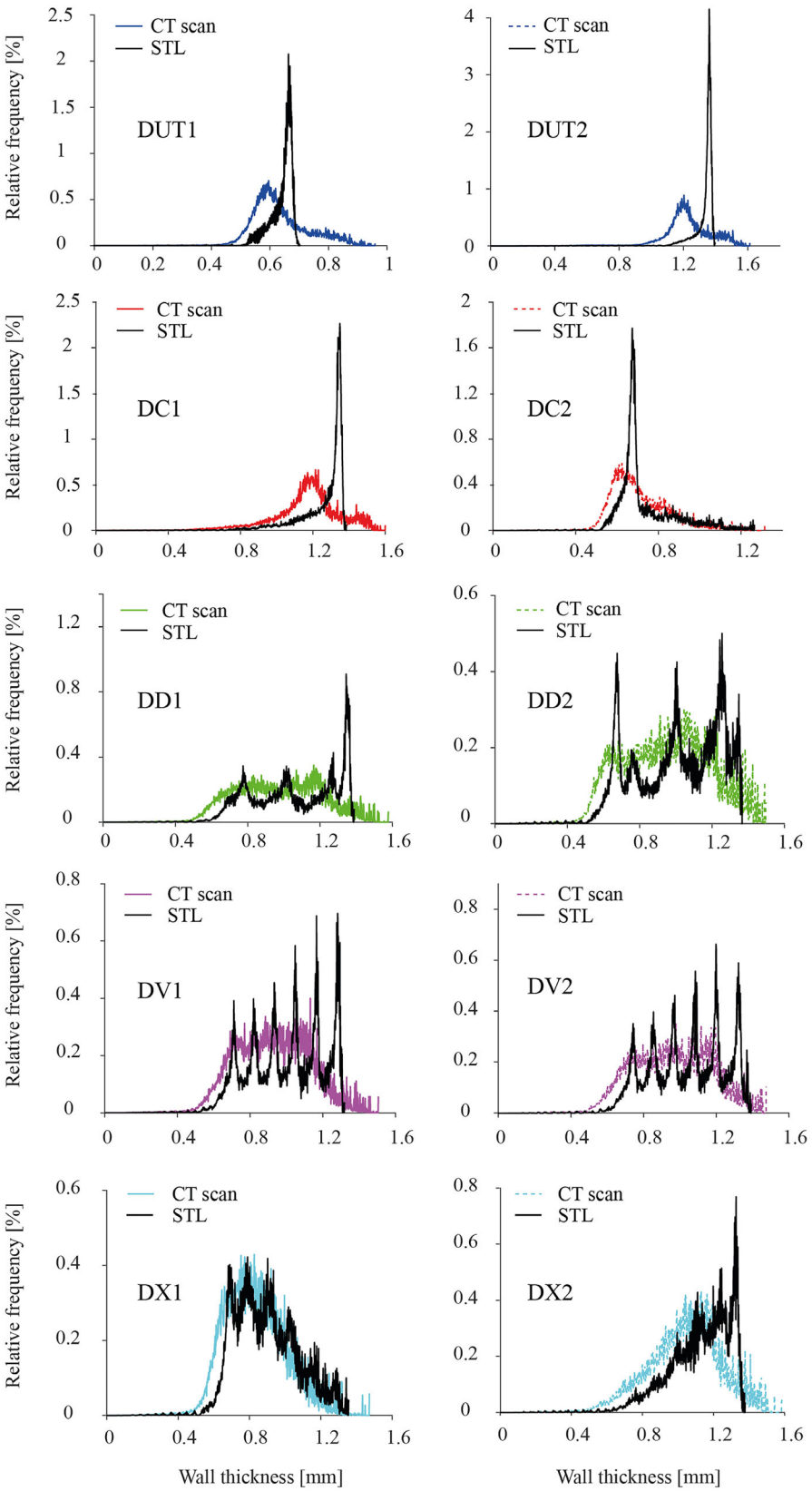


Figure 5. Wall thickness analysis results of the comparison between the distributions of the nominal STL geometries and the distributions obtained from CT scans.

© 2026 The Author(s). Advanced Engineering Materials published by Wiley-VCH GmbH

15272648, 2026, 5, Downloaded from https://advanced.onlinelibrary.wiley.com/doi/10.1002/adem.202502812 by Politecnico Di Torino Sist. Bibl Del Polit Di Torino, Wiley Online Library on [13/04/2026]. See the Terms and Conditions (https://onlinelibrary.wiley.com/terms-and-conditions) on Wiley Online Library for rules of use; OA articles are governed by the applicable Creative Commons License

Table 1. Mean (*M*) and SD values were calculated for the wall thickness distributions of the samples, and percentage differences (delta %) between the mean values.

Wall thickness	CT		STL		Delta [%]
	M [mm]	SD [mm]	*M* [mm]	SD [mm]	
DUT1	0.633	0.009	0.643	0.002	−1.5
DC2	0.696	0.019	0.722	0.019	−3.6
DX1	0.823	0.029	0.879	0.030	−6.3
DD2	0.929	0.056	0.999	0.054	−7.1
DV1	0.926	0.041	1.000	0.041	−7.4
DV2	0.946	0.046	1.026	0.043	−7.8
DD1	0.974	0.057	1.058	0.055	−8.0
DX2	1.040	0.042	1.127	0.030	−7.7
DC1	1.169	0.037	1.266	0.021	−7.7
DUT2	1.212	0.027	1.319	0.011	−8.1

internal channels intersect with the diagonal struts of the TPMS structure, as shown in Figure 4b. The extent of this thickening appears to increase with local wall thickness. **Figure 6** shows an example of the surface topography, with several powder particles partially melted on the surface of the structure, particularly the down-skin surface. The arrow in Figure 6 points at some of these powder particles, which can be identified as a possible reason behind the deviation of the wall thickness.

The difference between the nominal and the actual geometry is further corroborated by the nominal-to-actual comparisons shown in **Figure 7**. The relative and cumulative deviation distributions for all samples overlap, with the graded structures falling between the two uniform-thickness structures, DUT1 and DUT2. Specifically, DUT1 exhibited a peak deviation of −0.020 mm, while the denser DUT2 showed a peak at −0.057 mm. This consistent pattern may be interpreted as a systematic deviation or a characteristic signature of the manufacturing process. However, in the case of uniform structures such as DUT1 and DUT2 (exhibiting the lowest and highest relative densities, respectively), the deviation between the actual and nominal peak values remains ≈11%, despite a volume percentage deviation more than double in DUT2 compared to DUT1.

The core (DC) and cross (DX) graded structures exhibited behavior similar to that observed in structures with UT. At higher densities, higher discrepancies are observed in the deviation between the actual and nominal distributions (DX2 and DC1) compared to those found in specimens with lower thicknesses (DC2 and DX1).

Figure 7 also shows the cumulative deviation of the wall thickness. The trend of the cumulative deviation was found to be analogous to the relative deviation distribution, characterized by the cumulative deviation for DUT1 and DUT2 at the right and left extremes, respectively. The other structures with wall thickness gradation have a cumulative deviation intermediate between DUT1 and DUT2.

The cumulative deviation of all the samples produced, considered in an aggregate form, is characterized by a $D10 = -0.236 \pm 0.025$ mm, $D50 = -0.032 \pm 0.014$ mm, and $D90 = 0.225 \pm 0.012$ mm. In particular, the D10 value is higher in absolute terms, indicating a slightly larger negative deviation and greater dispersion compared to the positive deviations represented by D90. This happens for the samples DUT1 and DC2. These samples, characterized by the lowest values of relative densities, exhibit an asymmetric behavior in the left-hand region of the distribution, with maximum negative deviations not exceeding −0.35 mm as highlighted in Figure 7 (red circle).

3.2. Mechanical Properties and Mechanism of Deformation and Failure

Figure 8 displays the stress–strain curve for each geometry. These curves are obtained by averaging the data from the three

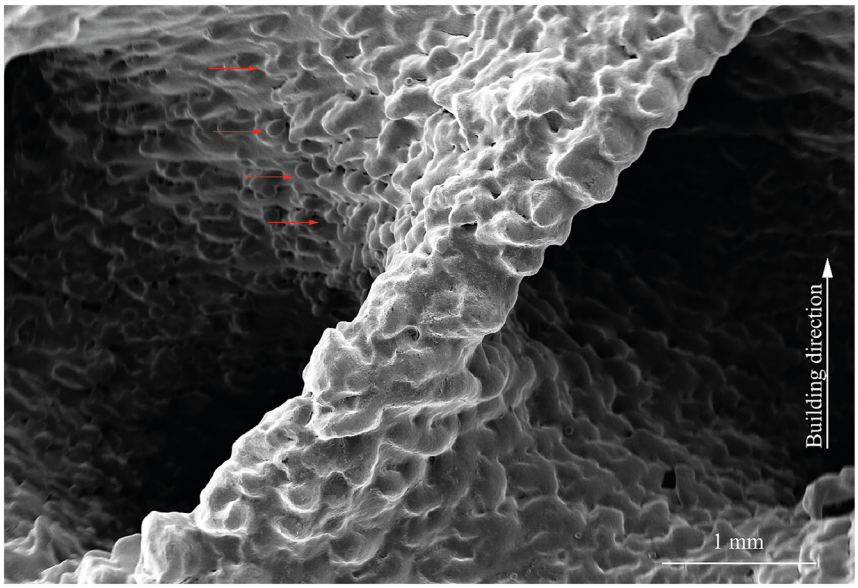


Figure 6. Surface topography of the produced samples. The red arrows indicate powder particles partially melted on the surface of the sample.

© 2026 The Author(s). Advanced Engineering Materials published by Wiley-VCH GmbH

15272648, 2026, 5, Downloaded from https://advanced.onlinelibrary.wiley.com/doi/10.1002/adem.202502812 by Politecnico Di Torino Sist. Bibl Del Polit Di Torino, Wiley Online Library on [13/04/2026]. See the Terms and Conditions (https://onlinelibrary.wiley.com/terms-and-conditions) on Wiley Online Library for rules of use; OA articles are governed by the applicable Creative Commons License

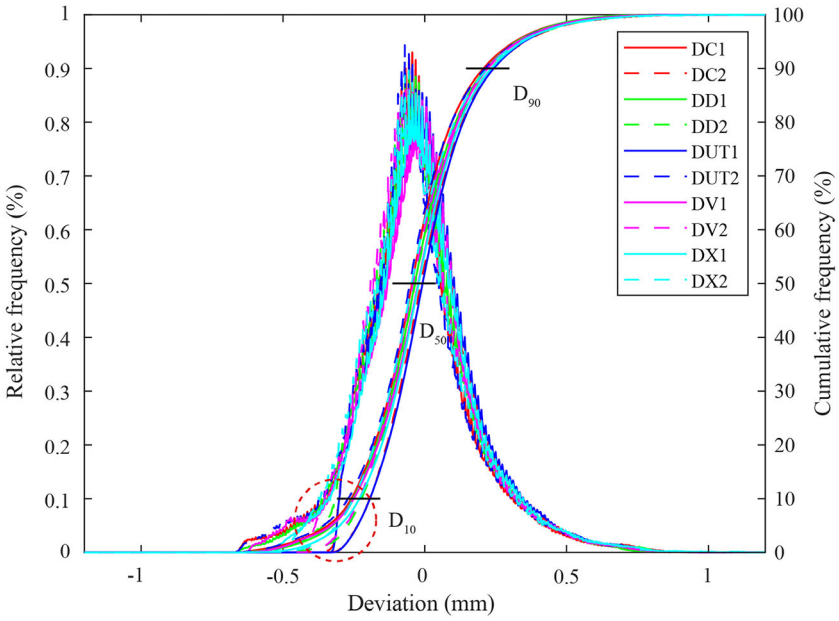


Figure 7. Relative deviations and cumulative deviations obtained from the nominal/Actual comparison analysis for the diamond structures considered in this work.

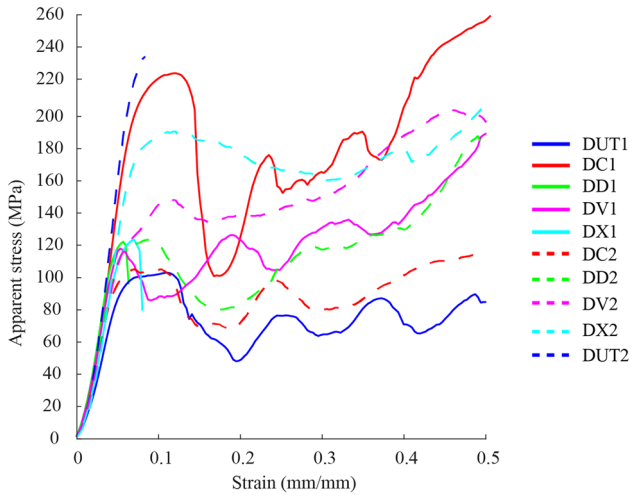


Figure 8. Stress–strain plots of the compression tests.

replicas of each geometry. Based on the relative densities of the structures, in agreement with the literature,[43,44] the stress–strain curves of the graded structures lie above the curve of the reference UT structure DUT1.

Table 2 reports the characteristic mechanical index for each structure according to ISO 13314:2011. The values are reported as mean and SD, based on the tests on the three replicas.

The data reveal a clear correlation between structural configuration and mechanical performance. Samples such as DC1 and DX2 stand out for their high compressive offset stress (σ_c), FMCS, and plateau stress (σ_{pl}), indicating superior load-bearing capacity and stability under compression. These samples also show the highest absorbed energy (W_{50}), suggesting enhanced energy dissipation capabilities. Conversely, DUT1 and DC2, with lower values across most parameters, reflect more limited mechanical efficiency. The quasielastic gradient follows a similar trend, reinforcing the influence of internal architecture and density on stiffness and overall mechanical response. The C and X type gradations, displaying quasielastic gradients of 2456 and about 3500 MPa respectively, resulted in the most and least stiff structures in the group with the thinnest initiator surface. The opposite occurred for the structures where the initiator surface was the thickest, with C and X gradations being the least and the most stiff, respectively (3946 MPa and 2823 MPa). **Figure 9** shows the corresponding Eulerian strain fields calculated along the compression axis obtained from DIC analyses. Both tensile and compressive strains coexist within each sample during loading. The local tensile strains observed under overall compressive loading originate from bending and shear deformation of the cell walls. This behavior is closely related to the local orientation of the TPMS surfaces with respect to the loading direction, which naturally leads to heterogeneous strain states throughout the structure. It should be emphasized that the tensile strains detected are significantly smaller in magnitude compared to the compressive strains. Although the color map may visually suggest comparable levels, the scale indicates that tensile strains are limited to values up to 0.05, while compressive strains reach values down to 0.20. **Figure 10** shows the deformation and failure of the structures during the compression test. Considering the strain in the thickness-graded structures, these exhibited an instability behavior similar to that of the UT structures. The structural collapse, which initiates at the FMCS, consistently occurs for the graded structures in the regions at lower relative densities. The failure initiation zones are localized in specific areas depending on the gradation patterns. The variable thicknesses within the geometry, based on the type of initiator

© 2026 The Author(s). Advanced Engineering Materials published by Wiley-VCH GmbH

15272648, 2026, 5, Downloaded from https://advanced.onlinelibrary.wiley.com/doi/10.1002/adem.202502812 by Politecnico Di Torino Sist. Bibl Del Polit Di Torino, Wiley Online Library on [13/04/2026]. See the Terms and Conditions (https://onlinelibrary.wiley.com/terms-and-conditions) on Wiley Online Library for rules of use; OA articles are governed by the applicable Creative Commons License

15272648, 2026, 5, Downloaded from https://advanced.onlinelibrary.wiley.com/doi/10.1002/adem.202502812 by Politecnico Di Torino Sist. Bibl Del Polit Di Torino, Wiley Online Library on [13/04/2026]. See the Terms and Conditions (https://onlinelibrary.wiley.com/terms-and-conditions) on Wiley Online Library for rules of use; OA articles are governed by the applicable Creative Commons License

Table 2. ISO 13314:2011 calculated mechanical performance indexes reported as the mean (M) values and the relative SD.

Sample	Quasi elastic gradient [MPa]		Compressive offset stress (σ_c) [MPa]		FMCS [MPa]		Plateau stress (σ_{pl}) [MPa]		Absorbed energy (W_{50}) [MJ m^{-3}]	
	M	SD	M	SD	M	SD	M	SD	M	SD
DUT1	2324.4	161.7	83.2	6.3	102.7	2.2	72.0	6.2	35.8	3.7
DUT2	4430.0	358.2	201.3	16.3	–	–	–	–	–	–
DC2	2456.0	160.9	86.6	5.4	107.3	3.3	87.7	7.2	43.6	3.2
DD2	2749.5	216.6	103.3	9.3	124.4	5.9	112.9	9.7	56.1	5.1
DV2	2840.0	162.1	108.2	8.4	150.5	6.4	146.5	11.2	72.9	4.9
DX2	3496.3	303.3	155.1	14.2	191.4	3.8	162.1	15.3	80.7	7.5
DC1	3945.8	322.4	178.6	15.8	225.7	1.8	162.6	13.3	86.2	8.3
DD1	3253.5	212.2	111.5	6.7	124.5	2.9	–	–	–	–
DV1	3066.3	243.0	111.7	7.3	129.6	7.0	118.3	8.6	58.9	3.8
DX1	2822.9	252.4	105.8	8.2	123.6	1.1	72.2	6.1	–	–

surfaces, perturb the layer-per-layer failure propagation mechanism. As a result, the failure modes that arise are contingent upon the gradation pattern that is implemented. The gradation pattern also influences the strain distribution in the samples. Structures such as the DV1 or DD1, characterized by thinner mid and diagonal regions, respectively, exhibit localized compression strains located at the thinner area, while the remaining area of the sample remains almost unloaded (orange). A detailed discussion of the structural behavior is provided below for each geometry. 1) In the case of uniform thickness structures (DUT), distinct mechanical behaviors were observed between DUT1 and DUT2. DUT2, designed with a nominal wall thickness of 1.4 mm, exceeded the load cell capacity of the tensile testing machine, reaching forces above 100 kN shortly before the FMCS. As a result, the test was interrupted prematurely. Conversely, DUT1, with a nominal thickness of 0.7 mm, exhibited more localized strain concentrations, both tensile and compressive, particularly at the junctions of the unit cells, as noticeable in Figure 9. These stress concentrations led to structural instabilities, manifesting as buckling and the formation of a horizontal shear band (Figure 10), ultimately causing the structure to collapse layer by layer. This behavior is consistent with previous findings in the literature[45] where such instabilities are associated with lower relative densities. The DIC contour plots in Figure 9 further illustrate the differences in deformation behavior. DUT2 shows a more uniform strain distribution, reflecting a smoother transition from elastic to plastic deformations. This is in line with the observations reported in,[46] which suggest that TPMS structures at higher relative densities tend to distribute loads more evenly. Additionally, the most stressed regions in DUT1 are located on surfaces inclined between 0° and 5° relative to the loading direction, areas particularly prone to stress accumulation due to their load-bearing capacity, as also noted by.[47] These regions are subjected to the highest compressive stress, visible in blue in the DIC maps, especially in the walls adjacent to the internal channels (Figure 9). 2) Core (DC). DC1 exhibited pronounced barreling during compression, indicative of significant lateral expansion. Following the FMCS, a noticeable stress drop was observed in the stress–strain curve, suggesting a sudden collapse of the initial load-bearing layers (visible in Figure 10). The subsequent plateau region displayed a progressively increasing slope (Figure 8), likely due to densification effects and the sequential engagement of stiffer regions. The failure mode was characterized by an initial layer-wise failure up to the longitudinal mid-line of the specimen, followed by the formation of a downward-oriented diagonal shear band (as marked in Figure 9 and 10). A secondary diagonal failure path emerged in the cells under the cells that failed first, indicating localized shear and sliding phenomena. In contrast, specimen DC2 did not exhibit barreling (Figure 10), suggesting a more uniform axial deformation. The strain distribution and the observed failure mode resemble those of the uniform structure with lower density, characterized by localized strain concentrations and high spatial gradients. Indeed, DC1 displays a more uniform strain distribution compared to DC2, once again consistent with findings in the literature for TPMS structures with higher densities.[46] The collapse initiated similarly with a layer-wise mechanism up to the specimen's mid-line, but the shear band propagated upward rather than downward. This was followed by a progressive, layer-by-layer failure, reflected in the stress–strain curve as a series of successive stress peaks (Figure 8). The plateau region was more stable compared to DC1, indicating a more controlled and gradual collapse. Notably, the lower-density region at the base of the specimen was the first to undergo a deformation, with a relatively uniform strain distribution across layers prior to FMCS. The stress drop after FMCS was significantly less pronounced than in DC1, suggesting a more energy-absorbing and stable collapse process. Considering the two DC structures, the central region played a key role. Changes in the relative density of the core of the structure perturb the layer-wise collapse mode typically observed in the uniform structures. The propagation direction of the diagonal shear band tends toward regions of lower density. In the case of DC1, it propagates downward toward the thinner core; conversely, in DC2, it propagates upward. 3) Diagonal (DD). Specimens DD1 and DD2 exhibited comparable values of FMCS and yield strength, despite DD1 demonstrating ≈20% higher stiffness. However, their post-yielding behavior diverged significantly due to differences in gradient orientation and structural configuration. DD1 failed in a brittle manner immediately after

 © 2026 The Author(s). Advanced Engineering Materials published by Wiley-VCH GmbH

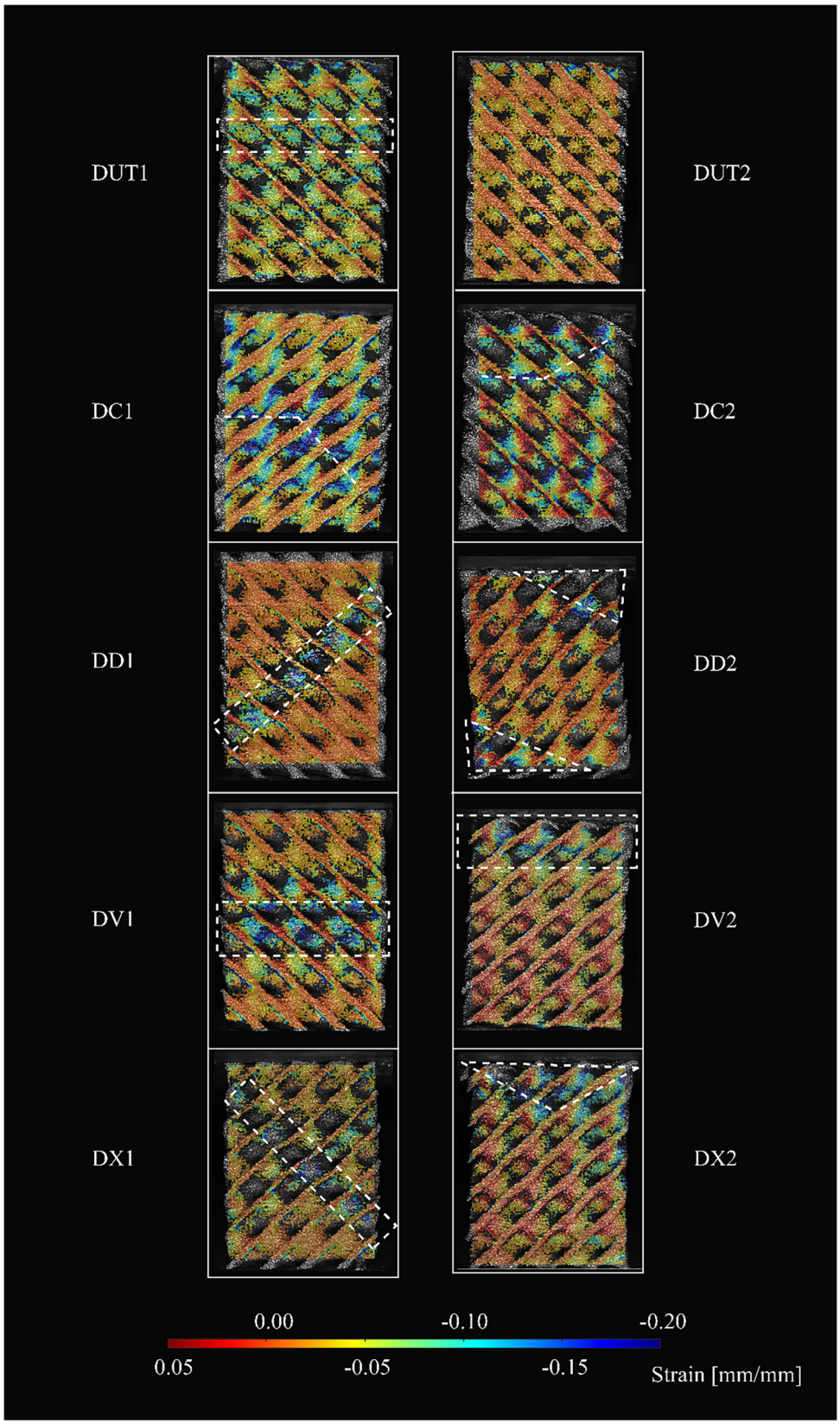


Figure 9. Eulerian longitudinal strain obtained from DIC analysis. The regions most highly stressed are highlighted in white, corresponding to the areas where strain concentration is more pronounced.

© 2026 The Author(s). Advanced Engineering Materials published by Wiley-VCH GmbH

15272648, 2026, 5, Downloaded from https://advanced.onlinelibrary.wiley.com/doi/10.1002/adem.202502812 by Politecnico Di Torino Sist. Bibl Del Polit Di Torino, Wiley Online Library on [13/04/2026]. See the Terms and Conditions (https://onlinelibrary.wiley.com/terms-and-conditions) on Wiley Online Library for rules of use; OA articles are governed by the applicable Creative Commons License

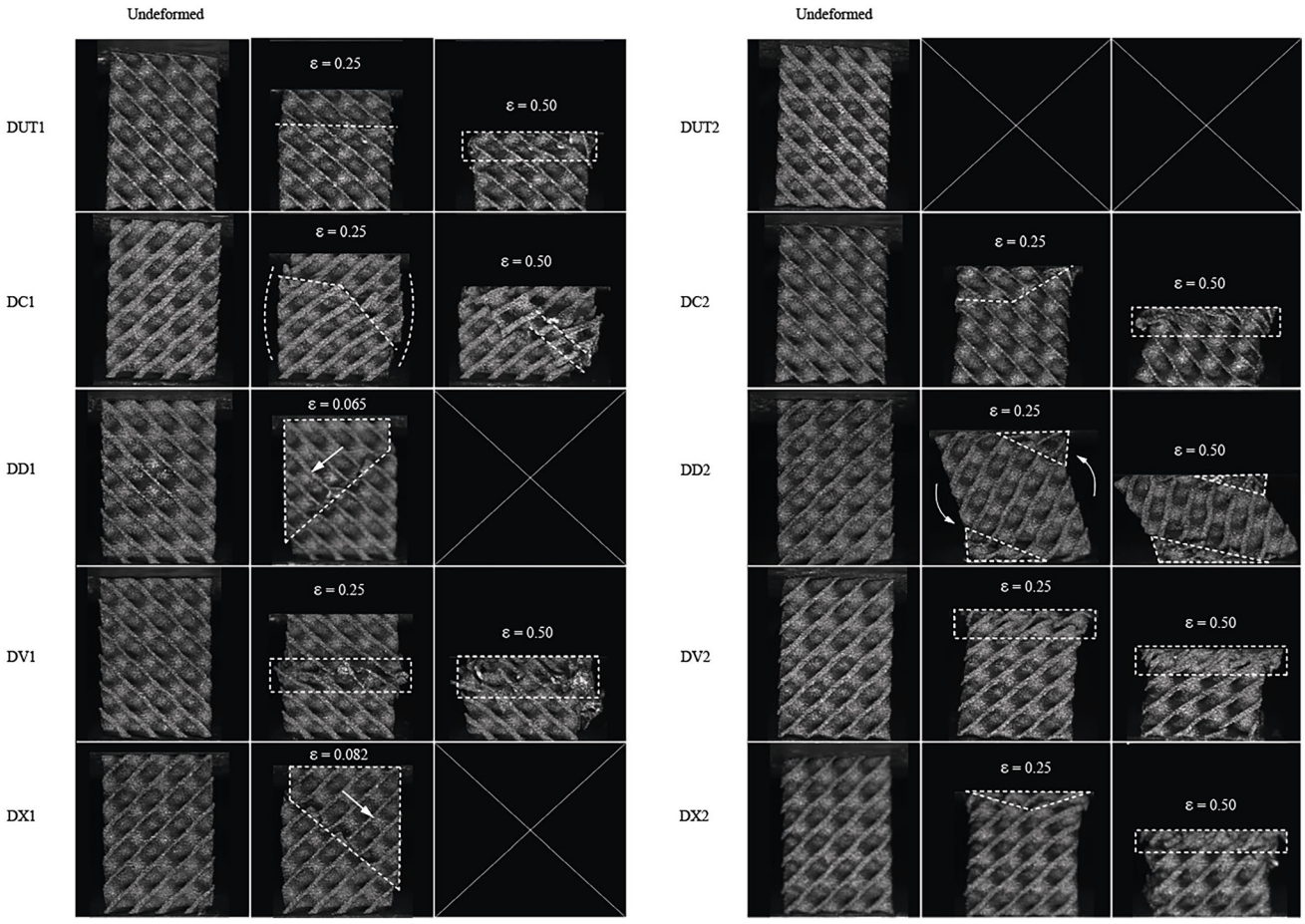


Figure 10. Deformation behavior and failure modes.

reaching its FMCS. The collapse initiated along the diagonal corresponding to the region of minimum wall thickness, as illustrated in Figure 9. This resulted in a complete separation of the specimen into two distinct halves, with no subsequent recovery of mechanical load-bearing capacity. The abrupt failure suggests a highly localized and catastrophic failure mode, dominated by the weakest gradient path. In contrast, DD2 exhibited a more progressive and stable deformation response. Failure initiated in the two triangular regions at lower density, located at the top-right and bottom-left corners of the specimen (Figure 9). As loading progressed, the specimen underwent a noticeable rotation under compression, as shown in Figure 10. The diagonal with a larger thickness of 1.4 mm gradually reoriented perpendicular to the loading direction, effectively redistributing the stresses and delaying the catastrophic failure. This behavior resulted in a modest stress drop following FMCS and a relatively stable plateau region in the stress–strain curve, indicative of a more ductile and energy-absorbing collapse mechanism. While the gradient of DD1 promoted early localization and brittle fracture, the configuration of DD2 enabled a more distributed deformation and enhanced post-yield stability. 4) Vertical (DV). DV1 exhibited noticeable barreling during compression, with failure initiating at the central layer of the specimen (blue region in Figure 9), which had the thinnest wall thickness. This was followed by a sequence of successive stress peaks in the stress–strain curve, indicative of the progressive layer-by-layer collapse mechanism, also visible in Figure 10. The deformation was localized in the central thinner region of the sample and evolved in a stepwise manner, with each layer contributing incrementally to the overall failure process. In contrast, DV2 exhibited a more uniform and stable deformation behavior. Failure initiated in the upper region at lower density (strain concentration in Figure 9) and propagated gradually, resulting in a smooth and continuous plateau in the stress–strain response, without the distinct stress peaks observed in DV1. This plateau reflects a significantly enhanced energy absorption capacity, approximately double that of the DV1 specimen. Comparing the FMCS of the two structures, DV2 reached FMCS at a higher strain level, with a peak stress ≈15% greater than that of DV1, despite having a nearly 7% lower quasielastic gradient. This suggests that the tailored gradient in DV2 effectively delayed the onset of failure and promoted a more efficient load redistribution. The collapse mode in DV2 remained layer-wise, similar to DV1, but was more evenly distributed and less abrupt, contributing to the improved mechanical performance. 5) Cross (DX). DX1 exhibited a failure mode similar to that of DD1, characterized by a sudden and brittle collapse along one

 © 2026 The Author(s). Advanced Engineering Materials published by Wiley-VCH GmbH

15272648, 2026, 5, Downloaded from https://advanced.onlinelibrary.wiley.com/doi/10.1002/adem.202502812 by Politecnico Di Torino Sist. Bibl Del Polit Di Torino, Wiley Online Library on [13/04/2026]. See the Terms and Conditions (https://onlinelibrary.wiley.com/terms-and-conditions) on Wiley Online Library for rules of use; OA articles are governed by the applicable Creative Commons License

15272648, 2026, 5, Downloaded from https://advanced.onlinelibrary.wiley.com/doi/10.1002/adem.202502812 by Politecnico Di Torino Sist. Bibl Del Polit Di Torino, Wiley Online Library on [13/04/2026]. See the Terms and Conditions (https://onlinelibrary.wiley.com/terms-and-conditions) on Wiley Online Library for rules of use; OA articles are governed by the applicable Creative Commons License

of the diagonals corresponding to the region of minimum wall thickness. This abrupt failure resulted in a complete loss of structural integrity, with no significant post-peak load-bearing capacity, as shown in Figure 9. In contrast, DX2 failed in a more progressive and controlled manner. The initial collapse occurred in the upper triangular region with lower density (Figure 9), followed by a layer-by-layer deformation sequence. This led to a horizontal plateau in the stress–strain curve, indicative of stable energy dissipation throughout the compression process. Notably, DX2 achieved an absorbed energy of up to 80.7 MJ m^{-3}, significantly outperforming DX1. Moreover, DX2 demonstrated a 25% higher stiffness and an FMCS ≈1.5 times greater than that of DX1. These results highlight the effectiveness of the specific gradient configuration in DX2 in enhancing both the structural stiffness and energy absorption capacity, while also promoting a more ductile and stable failure mode.

Figure 11 provides additional insights about the correlation between the geometry of the structure and the strain distribution. Figure 11a maps the angular deviation between the directional cosine of the surface and the build direction (*Z*-axis). In Figure 11a blue surfaces (90°) are aligned with the build direction, whereas horizontal surfaces (red, 0°) are orthogonal to it. Figure 11b displays the Lagrangian longitudinal strain at the FMCS region obtained from DIC analysis. Comparing Figures 11a,b shows a clear correspondence between the surface orientation and the strain concentration: vertical surfaces predominantly concentrate higher compressive strains, while horizontal surfaces are associated with tensile zones. This link is reinforced in the reported magnifications (Figure 11c,d), where the color-adjusted contour maps overlay visually correlating surface orientation and deformation response. The two boxed regions in Figure 11d highlight pronounced strain gradients along adjacent rib structures, alternating between zones of moderate and high compression (yellow and blue). These gradients suggest intense localized deformation, likely contributing to shear-dominated fracture pathways with cracks propagating obliquely across the ribs. Figure 11e represents an image of the sample under compression, and Figure 11f a magnification. Figure 11f illustrates additional failure modes: white lines indicate buckling and folding in compressed vertical regions, while red highlights mark zones of inter-rib sliding and rupture. Together, these insights suggest that surface orientation plays a decisive role in strain localization and failure evolution during mechanical loading, with a combination of buckling and shear responses shaping the final fracture patterns.

Figure 12a shows an optical microscopy image of the fracture surface of the sample DD1. For the area identified with a rectangle, Figure 12b,c shows SEM images of the fracture surface at low and high magnification, respectively. The fracture surfaces in Figure 12a are tilted from the orthogonal of the wall thickness. This is most likely the area of the samples where a shear stress concentration occurred. The failure angle is not homogeneous, and the differences are visible in Figure 12a, where the incident light of the optical microscope adopted is reflected directly toward the camera or deviated, according to the angle of the surface. Overall, the SEM image (Figure 12b) shows that the material does not have large internal defects or porosities, in agreement with the porosity results obtained from CT-scan analyses. The fracture surface shows the presence of large smooth surfaces (facets) and some regions with dimples. This is characteristic of a ductile-brittle failure mode. As noted by Sombatmai et al.,[47] reduced wall thickness facilitates crack propagation and limits plastic deformation, a behavior opposite to the typical behavior of the Ti6Al4V. The fracture morphology shown in Figure 12a,b indicates a mixed brittle–ductile failure mode, with initial instabilities triggered by shear banding in the thin-walled regions. The final rupture occurred at a surface defect acting as a local stress concentrator. In this area, the sample broke after a plastic deformation, visible as the equiaxed dimples on the surface.

In addition to their distinct mechanical responses, the investigated structures exhibit significant differences in energy absorption characteristics. **Figure 13** illustrates these properties, with Figure 13a,b showing the cumulative absorbed energy per unit volume and Figure 13c,d depicting the energy absorption efficiency. The reference uniform structure, DUT1, demonstrated an absorbed energy of 35.8 MJ m^{-3} at a global strain of 50%. Within the set of graded structures, DC2 showed the lowest cumulative energy absorption capacity, recording a value of 43.6 MJ m^{-3}, only slightly higher than that observed for DUT1. As presented in Table 2 and Figure 13c,d, the specimens can be categorized into two distinct groups based on their energy absorption capacity. This capacity generally correlates with the average relative density: specimens with higher relative density absorbed more energy. Exceptions to this trend include DD1 and DX1, which experienced brittle failure immediately after reaching the FMCS, and DUT2, for which testing was not feasible due to its strength exceeding the capacity of the testing apparatus. Higher energy absorption per unit volume is typically observed in specimens that fail progressively through multiple stages. This behavior was particularly evident in DV2 and DX2. Regarding energy absorption efficiencies (Figures 13c,d), among the specimens with the thinnest wall thickness at the initiator surface, DV1 exhibited slightly higher efficiency compared to DC1 and DUT1, both of which showed an overlapping trend. DV1 maintained superior efficiency to all the other structures up to ≈40% global strain, after which the efficiency reached a plateau at around 31%. DUT1, closely aligned with DC1, reached an efficiency of 35% at 50% strain. Within the structures with the thicker wall thickness at the initiator surface, DX2 and DV2 demonstrated the highest efficiencies, with DX2 reaching an efficiency of 40%. Their efficiency curves overlapped up to about 35% strain, beyond which DV2 exhibited an inflexion point, subsequently following a trend similar to DUT1. DD2, instead, mirrored the behavior of DC2 up to 40% strain, where it reached the highest efficiency of ≈32% before undergoing a marked decline. This drop is attributed to structural rotation under load, which compromises energy absorption efficiency by prematurely initiating densification. In fact, the peaks observed in the energy absorption efficiency curves correspond to the onset of densification, where the peak stress surpasses the corresponding FMCS values. At these strain levels, significant compaction occurs, re-establishing contact between the failed and heavily deformed regions and the remaining structure, thereby enhancing the load-bearing capacity.

A comprehensive comparison of the mechanical performance across the different gradation patterns considers the mass-normalized values of E_{spec}, $FMCS_{spec}$, and SEA (calculated as

 © 2026 The Author(s). Advanced Engineering Materials published by Wiley-VCH GmbH

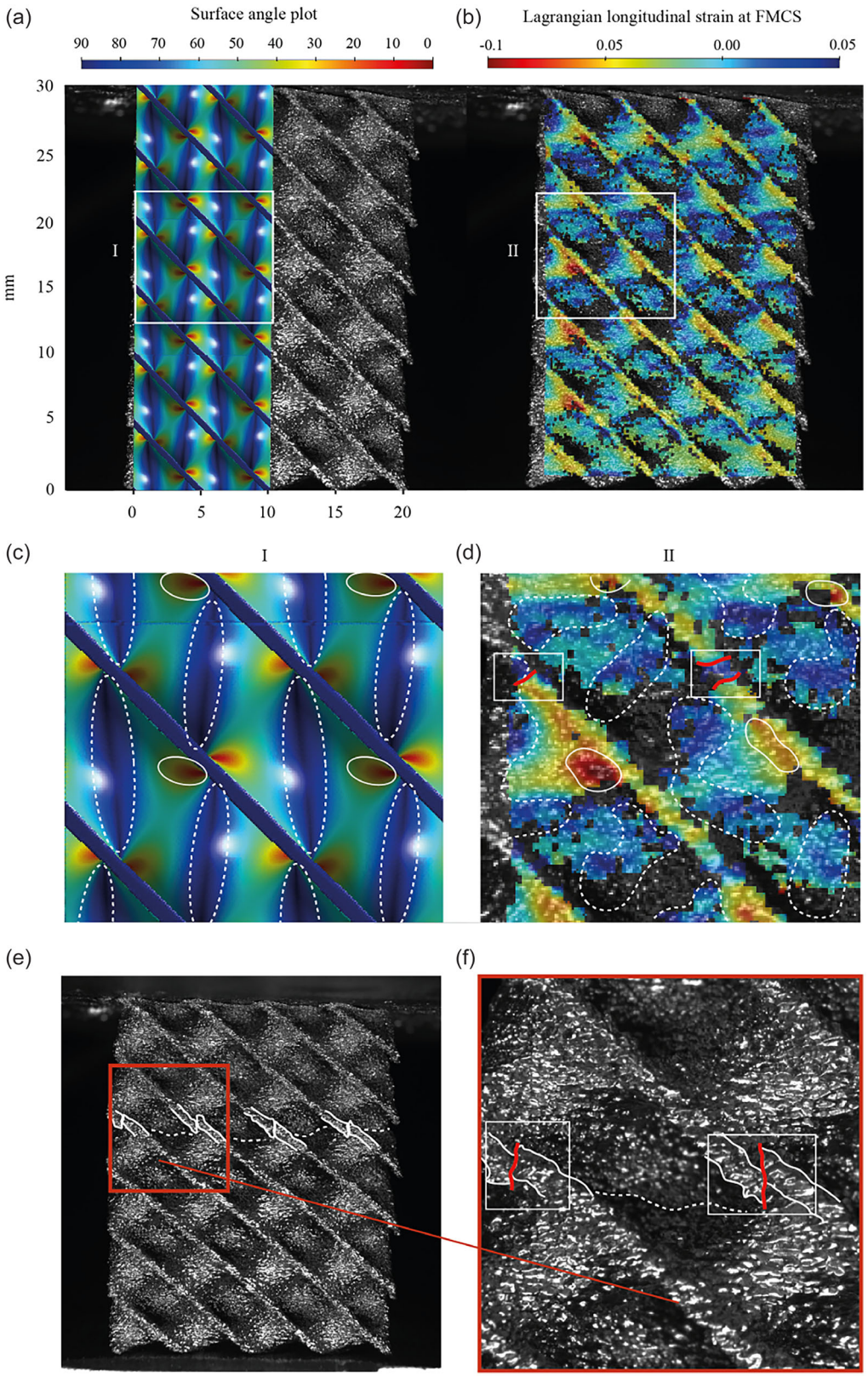


Figure 11. Comparison between the surface orientation of the structure and the strain location. a) A map of the angular deviation between the directional cosine of the surface and the build direction. b) The Lagrangian longitudinal strain at the FMCS region obtained from DIC analysis. c,d) magnification of the areas marked in (a,b) respectively. e) Image of the sample under compression and f) magnification with highlighted failure patterns.

© 2026 The Author(s). Advanced Engineering Materials published by Wiley-VCH GmbH

15272648, 2026, 5, Downloaded from https://advanced.onlinelibrary.wiley.com/doi/10.1002/adem.202502812 by Politecnico Di Torino Sist. Bibl Del Polit Di Torino, Wiley Online Library on [13/04/2026]. See the Terms and Conditions (https://onlinelibrary.wiley.com/terms-and-conditions) on Wiley Online Library for rules of use; OA articles are governed by the applicable Creative Commons License

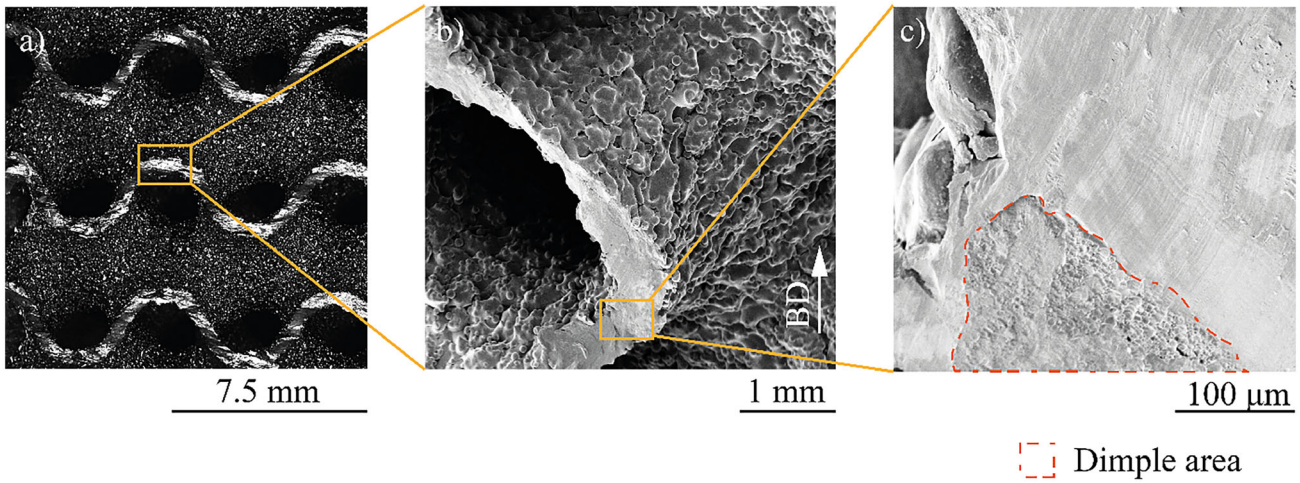


Figure 12. Fracture surface: a) Optical image of the total fracture surface. b,c) Local SEM images. In (b) BD is the build direction. In (c), the dashed area represents the location of the dimples.

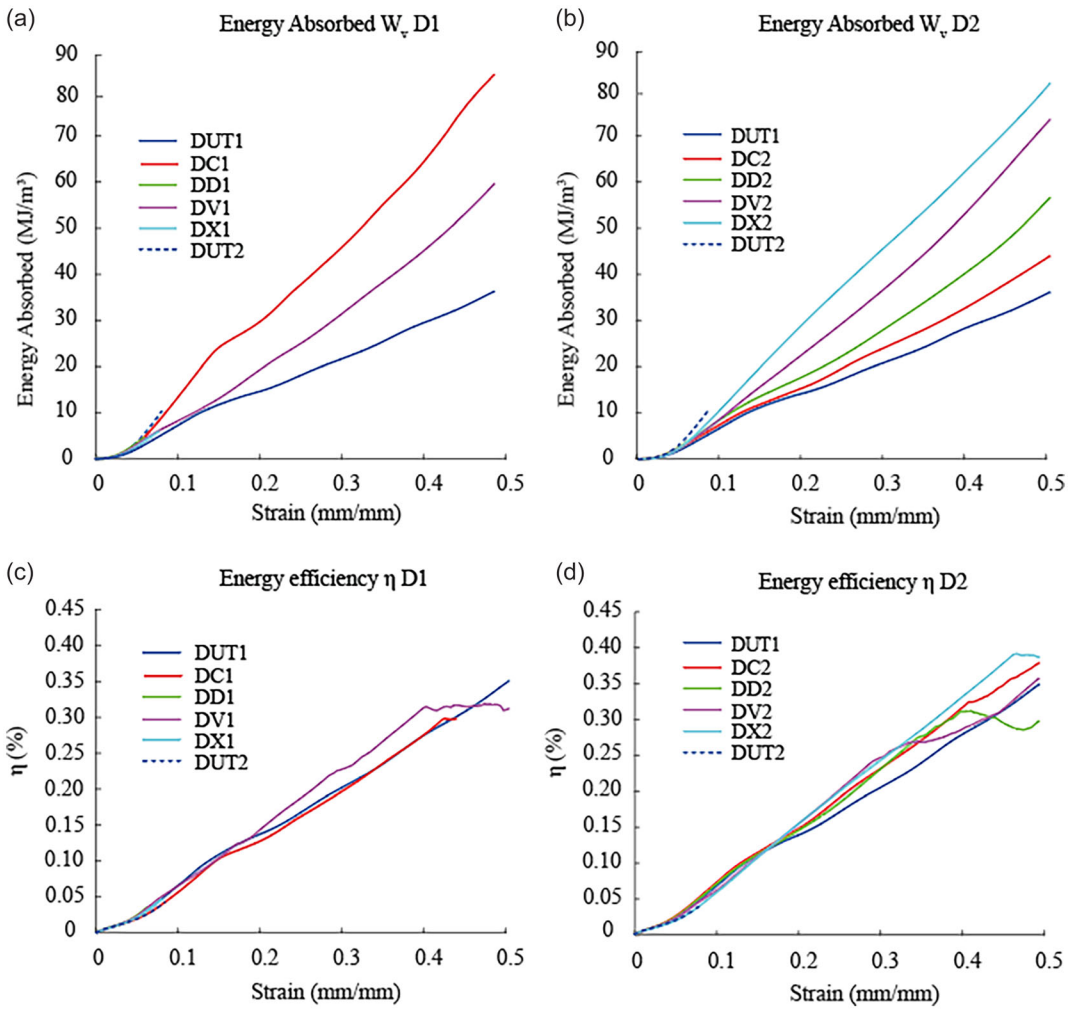


Figure 13. Cumulative energy absorption per unit volume and efficiency plots.

© 2026 The Author(s). Advanced Engineering Materials published by Wiley-VCH GmbH

15272648, 2026, 5, Downloaded from https://advanced.onlinelibrary.wiley.com/doi/10.1002/adem.202502812 by Politecnico Di Torino Sist. Bibl Del Polit Di Torino, Wiley Online Library on [13/04/2026]. See the Terms and Conditions (https://onlinelibrary.wiley.com/terms-and-conditions) on Wiley Online Library for rules of use; OA articles are governed by the applicable Creative Commons License

described in Section 2.4). These parameters are indicative of the resulting stiffness, strength, and crashworthiness capabilities of the structures. The specimens were grouped into three relative density clusters to minimize the influence of global density and emphasize the effect of internal gradation. The clusters are defined as follows: 1) Low-density group (blue in **Figure 14**): DC2 (relative density 0.24). 2) Medium-density group (orange in Figure 14): DD2 (0.32), DV1 (0.32), DV2 (0.33), and DD1 (0.33). 3) High-density group (gray in Figure 14): DX2 (0.36) and DC1 (0.41).

Samples DD1 and DX1 were excluded from the analysis as they failed catastrophically immediately after exceeding their FMCS.

Considering the E–SEA plot (Figure 14a), structures DC2 and DV2 exhibit the highest SEA values, identifying them as the most suitable candidates for applications where substantial energy absorption is required, such as the core of sandwich panels. Although both structures show comparable SEA, they belong to different relative density classes. In particular, DC2 has a lower relative density, making it especially attractive for applications where mass reduction is critical, such as aeronautical lightweight components. Moreover, DC2 displays an $E \approx 2.27 \times 10^6\ m^2\ s^{-2}$ that is larger than that of DV2 ($E \approx 1.97 \times 10^6\ m^2\ s^{-2}$), indicating that while both structures absorb approximately the same amount of energy (similar values of SEA), DC2 does so with smaller deformations. This behavior is likely associated with the presence of a thicker core region, which limits the deformation capacity and promotes a stiffer response. The absence of clear clustering by relative density in the E–SEA space further suggests that relative density is not the dominant parameter controlling the mechanical response of these graded TPMS structures. Instead, the specific wall-thickness gradation pattern plays a more decisive role.

A similar interpretation arises from the FMCS–SEA plot (Figure 14b), as an example, when comparing structures DD2 and DC1. Despite their comparable SEA values ($SEA \approx 10\ J\ g^{-1}$), DC1 exhibits a markedly larger elastic field ($FMCS \approx 0.125 \times 10^6\ m^2\ s^{-2}$), making it more suitable for applications where higher allowable loads prior to failure are required, for example, in lightweight structural elements. This difference again originates from the gradation strategy. The thinner regions in DD2 likely induce an early stress localization, drastically reducing its FMCS. Conversely, the FMCS of DC1 is less affected by the presence of a thinner spherical core, which is structurally

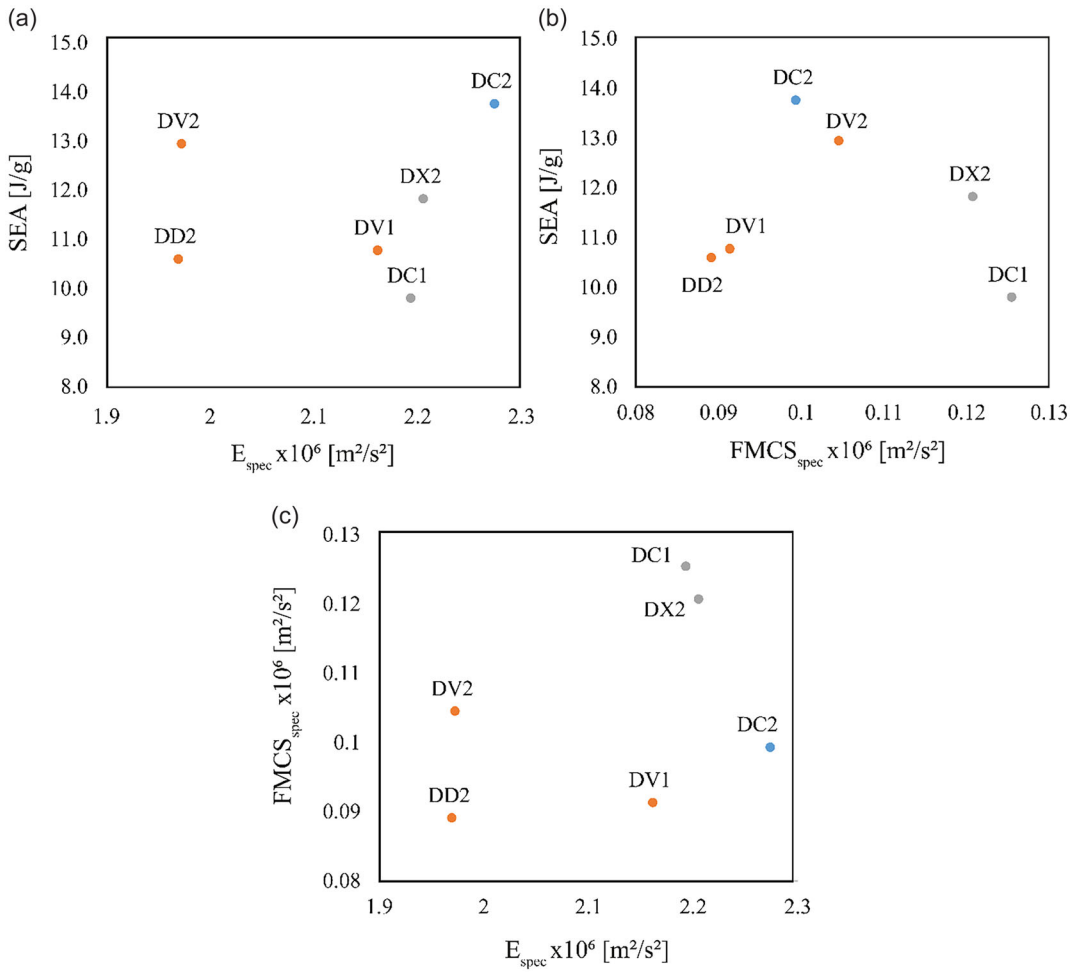


Figure 14. Comparative plots of the normalized performance parameters: a) E_{spec} – SEA, b) $FMCS_{spec}$ – E_{spec}, and c) E_{spec} – $FMCS_{spec}$.

© 2026 The Author(s). Advanced Engineering Materials published by Wiley-VCH GmbH

15272648, 2026, 5, Downloaded from https://advanced.onlinelibrary.wiley.com/doi/10.1002/adem.202502812 by Politecnico Di Torino Sist. Bibl Del Polit Di Torino, Wiley Online Library on [13/04/2026]. See the Terms and Conditions (https://onlinelibrary.wiley.com/terms-and-conditions) on Wiley Online Library for rules of use; OA articles are governed by the applicable Creative Commons License

15272648, 2026, 5, Downloaded from https://advanced.onlinelibrary.wiley.com/doi/10.1002/adem.202502812 by Politecnico Di Torino Sist. Bibl Del Polit Di Torino, Wiley Online Library on [13/04/2026]. See the Terms and Conditions (https://onlinelibrary.wiley.com/terms-and-conditions) on Wiley Online Library for rules of use; OA articles are governed by the applicable Creative Commons License

more efficiently supported by the surrounding material. Further insight is provided by the E–FMCS plot, particularly when examining structures DC1 and DV1. Although both present a similar stiffness of $E \approx 2.2 \times 10^6\,m^2\,s^{-2}$, their FMCS differ significantly: DC1 reaches $\approx 0.125 \times 10^6\,m^2\,s^{-2}$, whereas DV1 reaches only about $0.09 \times 10^6\,m^2\,s^{-2}$. This indicates that, despite sharing a thin-core configuration, their load-bearing capabilities differ substantially. The most plausible explanation lies in the geometry and spatial distribution of the thin regions. In DC1, the thin spherical core is centrally located and fully surrounded by thicker material, a configuration that mitigates its influence on the global structural resistance. In contrast, DV1 features an extended thin region spanning the entire cross-section at mid-height. This large, planar thin region collapses at lower loads and therefore governs the overall mechanical response.

The comparative analysis indicates that the most effective designs are not those that maximize a single mechanical attribute, but rather those that achieve an appropriate balance among stiffness, strength, and crashworthiness. Structures with very high stiffness tend to exhibit brittle, premature collapse and therefore offer limited energy absorption, whereas configurations optimized solely for SEA may lack the strength required to ensure structural integrity under load. The lack of any discernible clustering with respect to relative density in Figure 14 further confirms that density alone is not a sufficient predictor of mechanical performance for graded TPMS architectures. Instead, Figure 14 clearly demonstrates that the wall-thickness gradation pattern exerts a dominant influence on both the mechanical response and the deformation mechanisms, irrespective of the overall density.

4. Conclusions

This paper investigates the effect on surface morphology and mechanical properties under compression load of introducing 3D gradations of the wall thickness in lattice structures based on the diamond TPMS. The gradation (vertical (V), diagonal (D), cross (X), and core (C)) is realized by varying the thickness of the structure from a minimum thickness at the initiator surface (0.7 mm, named "1") to a maximum thickness (1.4 mm, named "2") and vice versa.

As expected, wall thickness gradation produced stress–strain curves that lie between those of the corresponding structures designed with UTs corresponding to the minimum or maximum thickness.

However, while the UT structures either fail linearly with compaction of the cells along the load direction (thinner structure DUT1) or do not fail (thicker structure DUT2), the graded structures exhibit a deformation behavior that is driven by the gradation pattern. The structures with a thinner central section (DC1 and DV1) show a barreling deformation before the failure. The structures characterized by a thin diagonal (DX1 and DD1) fail in a brittle manner, resulting in the complete separation of the structures into two distinct halves along the initiator surface. The structures with a thick diagonal, such as the DX2 and DD2, are characterized by a progressive failure located at the thinner areas of the structure, e.g., the triangular-shaped areas on top of the structure with cross gradation (DX2) or the corners of the structure with diagonal gradation (DD2). This behavior is explained by the energy absorption capability of the structures, which can be correlated to the relative density of the structure. The higher the density, the more energy is absorbed by the structure. The higher energy absorption was found in structures characterized by progressive failure, such as those with vertical gradation and a thicker core (DV2) and a cross gradation with larger thickness (DX2). This, however, comes with some exceptions, such as the structures with a thin diagonal (DD1 and DX1), which are characterized by a high relative density but fail in a brittle manner, thus absorbing less energy.

From the findings of this work, a few guidelines could be extracted to drive further development and design of such structures according to the design requirements. For example, to achieve a structure that collapses in a controlled manner, characterized by an extended plateau region and good energy absorption properties, it is preferred to use a structure with a thicker core (such as DC2, DV2, or DX2). These kinds of structures would be well-suited to sandwich panel applications. This would allow light structures with a controlled plate displacement or a controlled failure when compressed. Samples with the thinner core (DC1) and the thicker cross (DX2) showed the best performances in terms of compressive offset stress (σ_c), FMCS, plateau stress (σ_{pl}), and energy absorption capability (W_{50}). On the other hand, the structure with a thicker core (DC2) was the structure that showed the lowest mechanical properties among the wall thickness graduated samples. Overall, if a brittle fracture is preferred, a thin core or a thin diagonal (like the DC1, DD1, or the DX1) should be adopted. These structures may find applications as mechanical fuses, where the failure occurs when a specific load mode or value is reached. Structures like the DD1 or the DX1 may also find applications in other structures where a clean failure, without debris, is desired, such as in single-use medical devices (surgical tools), where detachment should not leave debris.

Overall, this study demonstrates that the grading of the wall thickness within TPMS-based lattice structures may be performed strategically to control the deformation and failure modes while also achieving an overall weight reduction, as the material is efficiently distributed to guide the fracture path and mode. This tailored distribution results in lightweight yet mechanically reactive structures capable of responding predictably and effectively to compressive loading. A further degree of freedom in the use of graded TPMS structures for tailoring deformation and failure mechanisms lies in the orientation of the applied load. Given the intrinsic geometric anisotropy of TPMS architectures, particularly in the case of 3D grading, different loading directions may activate distinct local and global deformation modes, leading to variations in stiffness, strength, and failure patterns. While the present study focuses on a single loading direction, future work may systematically explore the influence of loading orientation and combined loading states. Such investigations would not only deepen the understanding of direction-dependent behavior but also open opportunities for deliberately tuning the mechanical response of TPMS structures through the controlled alignment of load paths in design.

Appendix

Together with the data on stress and strain collected during the compression test, the 2D DIC technique was employed to

 © 2026 The Author(s). Advanced Engineering Materials published by Wiley-VCH GmbH

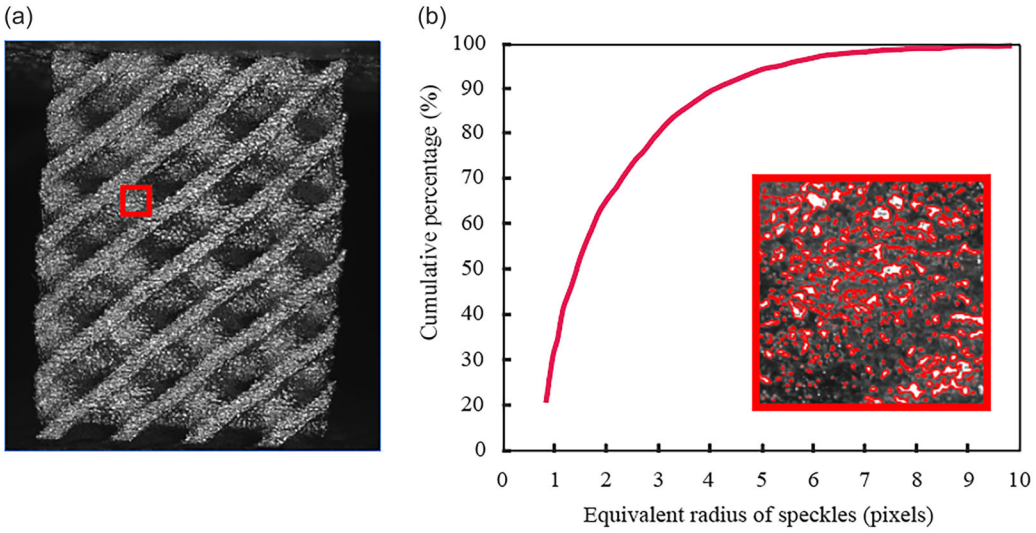


Figure A1. Speckle pattern characterization. a) Reference image and location of the speckle pattern analysis. b) Magnification of the area and the relative cumulative percentage plot of the area for the analysis.

investigate the deformation and failure modes of the samples. The DIC allows for following, at the part scale level, the strain field distribution during the compression test using multiple images acquired during the test, and analyzed using specific tools such as Ncorr,[48] a toolbox developed for MATLAB (MathWorks, Massachusetts, USA). The analysis of subsequent images during deformation is obtained by tracking specific reference points on the structure, typically created by applying a speckle pattern on the surface of the object. However, following the methodology proposed in other studies,[49,50] the DIC analysis was conducted without applying a speckle pattern, as the surface topography and roughness of the PBF-EB as-built surface reflect light, creating a natural speckle pattern adequate for the analysis. The images were acquired at a rate of 1 image per second and processed considering only a ROI. When performing such an analysis on complex structures, attention should be paid to the fact that, due to the complexity of the deformation, out-of-plane regions may appear, and the natural speckle pattern deforming with the structure pattern may change the light reflection during the deformation. These issues were overcome by identifying the ROI for the DIC analysis on the deformed state of the sample, after the compression test. The choice of the ROI, therefore, excluded the area of the samples where it was not possible to detect the speckle pattern. In addition, since the quality of the speckle pattern impacts the quality of the DIC analysis, it was preliminarily analyzed using a MATLAB script, which calculates three key parameters: the average speckle diameter, the minimum distance between speckles, and the total coverage area. The speckle diameter influences the spatial resolution. The average distance between speckles affects the ability to track the deformation with low correlation errors. The coverage area, defined as the ratio between the area covered by the speckles and the total area, impacts the contrast and effectiveness of the pattern. **Figure A1** a shows a DIC reference image adopted to evaluate the quality of the speckle pattern, while Figure A1b shows the relative cumulative percentage plot and the magnification of the area adopted for the evaluation of the quality of the pattern. From these analyses, a mean speckle diameter of 3.62 ± 1.84 pixels and an average minimum distance between the speckles of 5.76 ± 2.17 pixels were calculated. These values indicate a good quality of the speckle pattern according to the guidelines of the International Digital Image Correlation Society (iDICs),[51] which suggests an equivalent mean speckle diameter within the range of 3–5 pixels.[51,52] The coverage area of the speckle pattern of the structure was approximately equal to 26%. These data contributed to the choice of the subset radius. In DIC, the subset is defined as the region of pixels centered around each point of interest in the reference image. During the correlation process, the algorithm tracks how this subset moves and deforms between the undeformed and deformed images to calculate local displacements and strains. The choice of subset radius is critical because it must be large enough to contain a sufficient number of speckles for accurate correlation, but small enough to capture local strain gradients.[51] Based on these parameters, a subset radius of 12 pixels was selected for the DIC analysis. In this case, the chosen radius allowed accurate measurements at the sample scale and the correct identification of where the most considerable deformations occur.

The local strains along the loading direction, identified as Eulerian strain (ε), were used to analyze the deformation behavior of the structures. For the DIC analysis, a single deformation stage was selected for each structure, corresponding to the strain at the (ε_{FMCS}). This specific point was chosen as it represents the onset of structural instability and allows for a direct comparison of the critical strain localization sites and failure patterns in the structures.

Acknowledgements

Financed by the European Union - NextGenerationEU (National Sustainable Mobility Center CN00000023, Italian Ministry of University and Research Decree n. 1033 - 17/06/2022, Spoke 11 - Innovative Materials & Lightweighting). The opinions expressed are those of the authors only and should not be considered as representative of the

 © 2026 The Author(s). Advanced Engineering Materials published by Wiley-VCH GmbH

15272648, 2026, 5, Downloaded from https://advanced.onlinelibrary.wiley.com/doi/10.1002/adem.202502812 by Politecnico Di Torino Sist. Bibl Del Polit Di Torino, Wiley Online Library on [13/04/2026]. See the Terms and Conditions (https://onlinelibrary.wiley.com/terms-and-conditions) on Wiley Online Library for rules of use; OA articles are governed by the applicable Creative Commons License

European Union or the European Commission's official position. Neither the European Union nor the European Commission can be held responsible for them.

Open access publishing facilitated by Politecnico di Torino, as part of the Wiley - CRUI-CARE agreement.

Conflict of Interest

The authors declare no conflict of interest.

Data Availability Statement

The data that support the findings of this study are available from the corresponding author upon reasonable request.

Keywords

diamond, digital image correlation, electron beam melting, powder bed fusion with electron beam, X-ray tomography

Received: October 24, 2025
Revised: December 2, 2025
Published online: January 17, 2026

[1] C. Pan, Y. Han, J. Lu, *Appl. Sci.* **2020**, *10*, 6374.
[2] H. Yin, W. Zhang, L. Zhu, F. Meng, J. Liu, G. Wen, *Compos. Struct.* **2023**, *304*, 116397.
[3] Tauseef-ur-Rehman, H. M. Ali, M. M. Janjua, U. Sajjad, W.-M. Yan, *Int. J. Heat Mass Transfer* **2019**, *135*, 649.
[4] J. Liu, T. Chen, Y. Zhang, G. Wen, Q. Qing, H. Wang, R. Sedaghati, Y. M. Xie, *Compos. Struct.* **2019**, *208*, 385.
[5] G. Dong, Y. Tang, Y. F. Zhao, *J. Mech. Des.* **2017**, *139*, 100906.
[6] D. Bhate, *Materials* **2019**, *12*, 1060.
[7] D. Khrapov, M. Kozadayeva, A. Koptyug, T. Mishurova, D. Meinel, R. Surmenev, M. Surmeneva, *Mater. Today Commun.* **2023**, *35*, 106410.
[8] S. Hyde, Z. Blum, T. Landh, S. Lidin, B. W. Ninham, S. Andersson, K. Larsson, *The Language of Shape: The Role of Curvature in Condensed Matter: Physics, Chemistry and Biology*, Elsevier **1996**.
[9] H. Jia, H. Lei, P. Wang, J. Meng, C. Li, H. Zhou, X. Zhang, D. Fang, *Extreme Mech. Lett.* **2020**, *37*, 100671.
[10] J. Li, L. Wang, X. He, J. Liang, C. Dong, *Npj Adv. Manuf.* **2025**, *2*, 45.
[11] A. R. de Oliveira, A. de Andrade Mendes Filho, M. Masoumi, E. G. Del Conte, *Int. J. Adv. Manuf. Technol.* **2021**, *116*, 1271.
[12] H. Yin, X. Zheng, G. Wen, C. Zhang, Z. Wu, *Compos. Struct.* **2021**, *255*, 112897.
[13] E. A. A. Alkebsi, H. Ameddah, T. Outtas, A. Almutawakel, *Int. J. Comput. Integr. Manuf.* **2021**, *34*, 370.
[14] W. Li, G. Yu, Z. Yu, *Appl. Therm. Eng.* **2020**, *179*, 115686.
[15] L. Li, J. Shi, K. Zhang, L. Yang, F. Yu, L. Zhu, H. Liang, X. Wang, Q. Jiang, *J. Orthop. Transl.* **2019**, *19*, 94.
[16] H.-Y. Lei, J.-R. Li, Q.-H. Wang, Z.-J. Xu, W. Zhou, C.-L. Yu, T.-Q. Zheng, *Int. J. Hydrogen Energy* **2019**, *44*, 24782.
[17] F. M. Baena-Moreno, M. González-Castaño, J. C. Navarro de Miguel, K. U. M. Miah, R. Ossenbrink, J. A. Odriozola, H. Arellano-García, *ACS Sustainable Chem. Eng.* **2021**, *9*, 8198.
[18] Z. Lin, S. Dadbakhsh, A. Rashid, *J. Manuf. Processes* **2022**, *83*, 180.
[19] G. Rizza, M. Galati, *Int. J. Heat Mass Transfer* **2024**, *234*, 126055.
[20] C. Körner, *Int. Mater. Rev.* **2016**, *61*, 361.
[21] C. Polley, W. Radlof, F. Hauschulz, C. Benz, M. Sander, H. Seitz, *J. Mech. Behav. Biomed. Mater.* **2022**, *125*, 104882.
[22] D. Khrapov, A. Paveleva, M. Kozadayeva, S. Evsevleev, T. Mishurova, G. Bruno, R. Surmenev, A. Koptyug, M. Surmeneva, *Mater. Sci. Eng., A* **2023**, *862*, 144479.
[23] X. Peng, Q. Huang, G. Zhang, J. Li, X. Zhang, Y. Lu, Z. Jin, *Int. J. Mech. Sci.* **2022**, *226*, 107442.
[24] D. Khrapov, M. Kozadayeva, K. Manabaev, A. Panin, W. Sjöström, A. Koptyug, T. Mishurova, S. Evsevleev, D. Meinel, G. Bruno, D. Cheneler, R. Surmenev, M. Surmeneva, *Materials* **2021**, *14*, 4912.
[25] D. Khrapov, A. Koptyug, R. Surmenev, M. Surmeneva, *Mater. Today Commun.* **2024**, *40*, 109580.
[26] A. Ataee, Y. Li, D. Fraser, G. Song, C. Wen, *Mater. Des.* **2018**, *137*, 345.
[27] B. Sokollu, O. Gulcan, E. I. Konukseven, *Addit. Manuf.* **2022**, *60*, 103199.
[28] E. Bol, M. Ramulu, *J. Mater. Eng. Perform.* **2025**, *34*, 9037.
[29] A. du Plessis, N. Razavi, M. Benedetti, S. Murchio, M. Leary, M. Watson, D. Bhate, F. Berto, *Prog. Mater Sci.* **2022**, *125*, 100918.
[30] ISO 13314:2011 mechanical testing of metals—ductility testing—compression test for porous and cellular metals **2012**, https://www.iso.org/standard/53669.html (accessed February 20, 2025).
[31] F. Caiazzo, V. Alfieri, D. G. Guillen, A. Fabbricatore, *Int. J. Adv. Manuf. Technol.* **2022**, *123*, 2501.
[32] M. G. Gado, O. Al-Ketan, M. Aziz, R. A. Al-Rub, S. Ookawara, *Energy Technol.* **2024**, *12*, 2301287.
[33] O. Al-Ketan, D.-W. Lee, R. Rowshan, R. K. Abu Al-Rub, *J. Mech. Behav. Biomed. Mater.* **2020**, *102*, 103520.
[34] M. Galati, G. Rizza, S. Defanti, L. Denti, *Precis. Eng.* **2021**, *69*, 19.
[35] D. S. J. Al-Saedi, S. H. Masood, M. Faizan-Ur-Rab, A. Alomarah, P. Ponnusamy, *Mater. Des.* **2018**, *144*, 32.
[36] L. Yang, R. Mertens, M. Ferrucci, C. Yan, Y. Shi, S. Yang, *Mater. Des.* **2019**, *162*, 394.
[37] H. B. Qi, Y. N. Yan, F. Lin, R. J. Zhang, *Proc. Inst. Mech. Eng. B: J. Eng. Manuf.* **2007**, *221*, 1685.
[38] D. Kotzem, A. Höffgen, R. Raveendran, F. Stern, K. Möhring, F. Walther, *Prog. Addit. Manuf.* **2022**, *7*, 249.
[39] S. S. Al-Bermani, M. L. Blackmore, W. Zhang, I. Todd, *Metall. Mater. Trans. A* **2010**, *41*, 3422.
[40] M. Jamshidinia, R. Kovacevic, *Surf. Topogr. Metrol. Prop.* **2015**, *3*, 14003.
[41] C. J. Smith, F. Derguti, E. Hernandez Nava, M. Thomas, S. Tammas-Williams, S. Gulizia, D. Fraser, I. Todd, *J. Mater. Process. Technol.* **2016**, *229*, 128.
[42] C. Wang, C.-N. Sun, L. Zhang, S. Feih, P. Wang, *Virtual Phys. Prototyp.* **2024**, *19*, e2430319.
[43] E. Onal, J. E. Frith, M. Jurg, X. Wu, A. Molotnikov, *Metals* **2018**, *8*, 200.
[44] X. Fan, Q. Tang, Q. Feng, S. Ma, J. Song, M. Jin, F. Guo, P. Jin, *Int. J. Mech. Sci.* **2021**, *204*, 106586.
[45] P. Khanna, S. Sood, P. Mishra, V. Bharadwaj, A. Aggarwal, S. J. Singh, *Structures* **2024**, *64*, 106580.
[46] I. Mat Samudin, N. A. Mohd Radzuan, A. B. Sulong, Q. Ma, A. H. Azman, W. F. H. Wan Zamri, *J. Mater. Res. Technol.* **2025**, *36*, 5757.
[47] A. Sombatmai, K. Tapracharoen, V. Uthaisangsuk, S. Msolli, P. Promoppatum, *Results Eng.* **2024**, *23*, 102364.

 © 2026 The Author(s). Advanced Engineering Materials published by Wiley-VCH GmbH

15272648, 2026, 5, Downloaded from https://advanced.onlinelibrary.wiley.com/doi/10.1002/adem.202502812 by Politecnico Di Torino Sist. Bibl Del Polit Di Torino, Wiley Online Library on [13/04/2026]. See the Terms and Conditions (https://onlinelibrary.wiley.com/terms-and-conditions) on Wiley Online Library for rules of use; OA articles are governed by the applicable Creative Commons License

[48] J. Blaber, B. Adair, A. Antoniou, *Exp. Mech.* **2015**, *55*, 1105.
[49] N. Vanderesse, A. Richter, N. Nuño, P. Bocher, *J. Mech. Behav. Biomed. Mater.* **2018**, *86*, 397.
[50] W.-M. Chen, Y. M. Xie, G. Imbalzano, J. Shen, S. Xu, S.-J. Lee, P. V. S. Lee, *Int. J. Precis. Eng. Manuf.* **2016**, *17*, 793.
[51] E. Jones, M. Iadicola, R. Bigger, B. Blaysat, C. Boo, M. Grewer, J. Hu, A. Jones, M. Klein, P. Lava, M. Pankow, K. Raghavan, P. Reu, T. Schmidt, T. Siebert, M. Simonsen, A. Trim, D. Turner, A. Vieira, T. Weikert, *A Good Practices Guide for Digital Image Correlation*, 1st ed., International Digital Image Correlation Society **2018**, https://doi.org/10.32720/idics/gpg.ed1/print.format.
[52] D. Lecompte, A. Smits, S. Bossuyt, H. Sol, J. Vantomme, D. Van Hemelrijck, A. M. Habraken, *Opt. Lasers Eng.* **2006**, *44*, 1132.

© 2026 The Author(s). Advanced Engineering Materials published by Wiley-VCH GmbH

15272648, 2026, 5, Downloaded from https://advanced.onlinelibrary.wiley.com/doi/10.1002/adem.202502812 by Politecnico Di Torino Sist. Bibl Del Polit Di Torino, Wiley Online Library on [13/04/2026]. See the Terms and Conditions (https://onlinelibrary.wiley.com/terms-and-conditions) on Wiley Online Library for rules of use; OA articles are governed by the applicable Creative Commons License